

Wood-Derived Fe Cluster Reinforced Asymmetric Single-Atoms Catalysts and Weather-Resistance Organohydrogel for Wide Temperature Flexible Zn-Air Batteries

Jiachuan Chen[#], Chenglong Qiu[#], Lei Zhang^{}, Baobin Wang, Penghua Zhao, Yu Zhao, Huanlei Wang^{*}, Guihua Yang^{*}, Aoran Sun, Jiaming Fan, Qixi Xv, Orlando J. Rojas^{*}*

Jiachuan Chen, Chenglong Qiu, Lei Zhang, , Baobin Wang, Penghua Zhao, Yu Zhao, Guihua Yang, Aoran Sun, Jiaming Fan, Qixi Xv

State Key Laboratory of Biobased Material and Green Papermaking, Qilu University of Technology, Shandong Academy of Sciences, Jinan 250353, PR China

zaozhizhanglei@163.com; ygh2626@126.com

Chenglong Qiu, Huanlei Wang

School of Materials Science and Engineering, Ocean University of China, Qingdao 266100, China huanleiwang@ouc.edu.cn

Orlando J. Rojas

Bioproducts Institute, Department of Chemical & Biological Engineering, Department of Chemistry, and Department of Wood Science, 2360 East Mall, The University of British Columbia, Vancouver, BC V6T 1Z3, Canada Orlando.rojas@ubc.ca

S1. Experimental Details

Chemicals and Reagents: Ferric chloride hexahydrate ($\text{FeCl}_3 \cdot 6\text{H}_2\text{O}$), ammonium chloride (NH_4Cl), potassium hydroxide (KOH), sodium hydroxide (NaOH), sodium sulfite (Na_2SO_3), zinc acetate [$\text{Zn}(\text{CH}_3\text{COO})_2$], Nafion-117, and PVA were purchased from Aladdin Scientific Corporation, California, USA. Sinopharm Chemical Reagent Co., Ltd. provided the ethyl alcohol ($\text{C}_2\text{H}_5\text{OH}$) and hydrogen peroxide (H_2O_2), China. Dimethyl sulfoxide (DMSO) was acquired from Kangde Chemical Co., Ltd., China. Carbon cloth was purchased from Phychemi Co. Ltd., Hongkong, China. Eucalyptus plants were provided by a paper factory in Shandong, China. All chemical reagents were utilized directly without prior purification.

Preparation of black liquor and cellulose pulp: The eucalyptus wood was subjected to hydrolysis by 2.5 M NaOH /0.4 M Na_2SO_3 solution in a digester at 171 °C for 2 h, with a dosage of 10 g eucalyptus and 50 mL of the aforementioned solution. The resulting pulp can be utilized for papermaking or other cellulose materials (cellulose was employed to enhance the PVA-based organohydrogel in this study). Pulping Black liquor (PBL) is accumulated for subsequent catalyst preparation purposes.

Synthesis of Fe_2O_3 -SC: In total, the pH of PBL was adjusted to approximately 7.4 by adding 9 M HCl until the desired pH level was reached and resulting in solution A. Subsequently, a uniform black suspension known as solution B was generated by ultrasonication for 30 min after adding 5 mL of an aqueous solution containing 0.5 g of $\text{FeCl}_3 \cdot 6\text{H}_2\text{O}$ to solution A. Solution B was subsequently subjected to freeze-drying and pyrolysis at a temperature of 900 °C for 2 h (heating rate of 5 °C/min) in a tube furnace

under nitrogen atmosphere. Finally, the Fe₂O₃-SC was obtained by vacuum drying at 60 °C for 12 hours after washing to remove sodium chloride.

Synthesis of Fe_x/FeN₃S₁-C: The Fe₂O₃-SC was ground completely with NH₄Cl (mass ratio Fe₂O₃-SC to NH₄Cl of 1:20) and the resulting powder was placed in a crucible at 900 °C under nitrogen atmosphere to obtain Fe_x/FeN₃S₁-C. For comparison, the ground powder was heated at either 800 or 1,000 °C, denoted as Fe_x/FeN₃S₁-C-800 and Fe_x/FeN₃S₁-C-1000, respectively. The FeN₃S₁-C without Fe clusters was fabricated by stirring and washing the Fe_x/FeN₃S₁-C with 1 M HCl at 80 °C for 12 h. The NSC was obtained using solution A prepared through the same methods as for Fe_x/FeN₃S₁-C, except for the addition of ferric chloride. S-C was prepared by freeze-drying solution A, directly followed by pyrolysis at 900 °C under nitrogen atmosphere.

Material characterization: SEM (Zeiss EVO-18,10KV, Zeiss Group, Germany), TEM (FEI Talos F200X, ThermoFischer Scientific, Massachusetts, USA), and HR-TEM (FEI Themis Z 300 KV, ThermoFischer Scientific, Massachusetts, USA) were utilized to analyze the morphology of the catalyst. Raman spectra datasets were collected employing a Renishaw in Via microscope (Renishaw plc, Gloucestershire, England). The structural composition of the sample was examined using the X-ray absorption spectra (XAS, Beijing Synchrotron Radiation Facility (BSRF)), determined X-ray diffraction (XRD; Rigaku Ultima IV, Rigaku Corporation, Japan), X-ray photoelectron spectroscopy analysis (XPS, ThermoFischer Scientific, Massachusetts, USA). Nitrogen adsorption at 77 K was used to determine the Brunauer-Emmett-Teller (BET) specific surface area using a surface area and porosity analyzer (Kubo X1000).

Electrochemical Measurements: The electrocatalytic activity of ORR was evaluated using a CHI 760E workstation (CHI Instruments, Shanghai, Chenhua, China) in a conventional three-electrode system, with platinum foil serving as the counter electrode and Ag/AgCl serving as the reference electrode. To prepare the working electrode, 5 mg of catalyst was added to 1 mL Nafion ethanol solution (990 μL ethanol combined with 10 μL Nafion). A homogenous ink was then achieved by continuous ultrasonic dispersion for 30 minutes. Subsequently, a 5 mm-diameter glassy carbon electrode was meticulously coated with 10 μL of catalyst ink, resulting in an approximate catalyst loading of 255 $\mu\text{g cm}^{-2}$. The same method was employed to prepare a catalyst for the commercial Pt/C (20 wt%) catalyst solution. Cyclic voltammogram (CV) curves were recorded in a 0.1 M KOH solution with N_2 - or O_2 -saturation at 0.2–0.8 V and 50 mV s^{-1} . The rotating ring disk electrode (RRDE) technology was employed at several rotational speeds between 400 to 2025 rpm with a scanning rate of 10 mV s^{-1} . To evaluate its long-term stability, $\text{Fe}_x/\text{FeN}_3\text{S}_1\text{-C}$ was tested at a constant voltage (–0.4 V vs. Ag/AgCl) and rotational speed of 900 rpm in an O_2 -saturated electrolyte containing 0.1 M KOH.

The Koutecky-Levich equation was used to determine the number of electrons transported (n) by the slope of its best linear fit line as follows:

$$\frac{1}{j} = \frac{1}{j_k} + \frac{1}{B\omega^{1/2}} \quad (1)$$

where j , ω , and j_k stand for the measured current, electrode rotation rate and kinetic-limiting current, respectively.

The following computation was used to determine the theoretical Levich slope (B):

$$B = 0.62nFC_{O_2}D_{O_2}^{2/3}v^{-1/6} \quad (2)$$

where n , C_{O_2} , F , v , and D_{O_2} denote the transfer electron number, the oxygen concentration (solution) ($1.2 \times 10^{-6} \text{ mol cm}^{-3}$), the Faradaic constant (96485 C mol^{-1}), the kinematic viscosity of the 0.1 M KOH ($0.01 \text{ cm}^2 \text{ s}^{-1}$) and the oxygen diffusion coefficient ($1.9 \times 10^{-5} \text{ cm}^2 \text{ s}^{-1}$).

The following formulas were used to calculate the H_2O_2 yield and electron transfer number (n), which were used to assess the catalysts' four-electron selectivity.

$$n = 4 \times \frac{I_D}{I_D + I_R/N} \quad \text{and} \quad (3)$$

$$\%(H_2O_2) = 200 \times \frac{I_R/N}{I_D + I_R/N} \quad (4)$$

where N represents the current collecting efficiency of the Pt ring, with a value of 0.37,

I_D and I_R denote the disk and ring currents, correspondingly.

All potentials obtained using Ag/AgCl as the reference electrode were converted to RHE in accordance with established protocols:

$$E_{RHE} = E_{Ag/AgCl} + 0.0591pH + E_{Ag/AgCl}^0 \quad (5)$$

where $E_{Ag/AgCl}$ is the measured potential and $E_{Ag/AgCl}^0 = 0.197 \text{ V}$.

Assembly of aqueous rechargeable Zn–air batteries (ZABs): Rechargeable ZABs were fabricated using a two-electrode configuration, in which the $\text{Fe}_x\text{-FeN}_3\text{S}_1\text{-C}$ catalyst was coated uniformly onto a carbon cloth to serve as air cathode (loading of 1 mg cm^{-2}). The polished Zn foil with an area of $1 \times 1 \text{ cm}^2$ and a thickness of 0.3 mm was used as the active anode. The electrolyte employed comprised a 6 M KOH solution supplemented with a 0.2 M $\text{Zn}(\text{Ac})_2$ solution.

All the measurement methods for the ZABs were tested at a temperature of $25 \text{ }^\circ\text{C}$

using an electrochemical workstation (CHI 760E). LSV was employed to measure polarization curves at 5 mV s^{-1} . The stability assessment of charge–discharge cycles was conducted using recurrent galvanized pulses (Landt-CT2001A).

The following formula was used to get the specific capacity:

$$C = \frac{I \times t}{m}, \quad (6)$$

where the mass loading of the consumed Zn anode is expressed as m (g cm^{-2}), the discharge duration is expressed as t (h), and the current density is expressed as I (mA cm^{-2}). The ZABs' power density (P) was computed using the following formula:

$$P = I \quad (7)$$

where the corresponding potential is denoted by V and the discharge current density by I . The energy efficiency (η) of the ZABs was computed based on the ratio between the discharge specific energy (Q_d) of the cell and the charge specific energy (Q_c):

$$\eta = \frac{Q_d}{Q_c} \times 100\%. \quad (8)$$

Preparation of C-CNFS: Cationic cellulose nanofibers (C-CNFS) were obtained following a previous study published in *C, L Qiu et al Industrial Crops and Products (Volume 186, page 115242, 2022)*. In a typical synthesis process, the raw pulp was subjected to thorough purification with hydrogen peroxide to effectively remove lignin and heteropolysaccharides. Subsequent filtration and drying steps produced highly pure cellulose pulp. Cationic nanocellulose was synthesized through a cationization strategy combined with high-pressure homogenization. N-(2,3-epoxypropyl) trimethylammonium chloride (EPTMAC) was employed as cationizing agents during this process. In particular, 15 g of water was used to dissolve 7.5 g of EPTMAC and

2.25 g of NaOH, followed by the addition of 60 g aqueous dispersion containing cellulose pulp at a concentration of 25%. The mixture was then completely dispersed to achieve a uniform reaction system consisting of cellulose and chemicals. 180 g of isopropanol was used to dilute this mixture, which was then agitated for three hours at 50 °C. By using centrifugation, unreacted reagents and byproducts were successfully removed. Subsequently, after a complete dialysis in distilled water for 72 hours (with a molecular cutoff value of 14,000), the resulting cationic slurry was rinsed with distilled water. During this process, the distilled water is changed every 3 hours for the first 24 hours and three times for the subsequent 48 hours. Finally, the resulted product was then filtered and refrigerated at 4 °C for future experimentation.

Preparation of CNF@PVA-SSE and PVA-SSE: During the synthesis of organohydrogel, a suspension of aqueous cationic cellulose nanofibers (6 g, 1.26 wt. %) was introduced into dimethyl sulfoxide (15 g) and subjected to agitation for 2 h to obtain a homogeneous solution of cationic cellulose (referred to as solution C). Subsequently, polyvinyl alcohol (1.8 g) was blended with solution C and heated to 90 °C while being stirred continuously until the complete dissolution of PVA. The resulting CNF-PVA mixed solution was allowed to settle without stirring to eliminate any trapped air bubbles. The transparent solution was applied to the PTFE mold and allowed to gel at –20 °C for 12 h, resulting in the formation of CNF@PVA hydrogel. For the preparation of PVA hydrogel, cationic-CNF was replaced with deionized water (5.868 g) while the other procedures were consistent. Subsequently, the hydrogel was prewetted with 6 M KOH/0.2 M Zn(CH₃COO)₂ in a vacuum chamber for 12 h. The

preparation of CNF@PVA-hydrogel/PVA-hydrogel followed a procedure similar to that for CNF@PVA-SSE, except that DMSO was substituted with H₂O.

Assembly of wide temperature flexible rechargeable ZABs: Using polished Zn foil as the anode, carbon cloth with Fe_x/FeN₃S₁-C as the air cathode, and CNF@PVA-SSE as the electrolyte, a rechargeable flexible ZABs was fabricated.

Computational method: Density functional theory (DFT) calculations were conducted using quantum expression (QE)^{1,2} within the framework of the pseudopotential plane wave (PPW) method. To account for the exchange correlation effects of electrons, we employed the Perdew–Buek–Ernzerhof (PBE) functional.³ The ionic cores were described using projected augmented wave (PAW) potentials,^{4,5} while the valence electrons were considered with a plane basis set, and a kinetic energy cutoff of 50 Ry was applied.

To assess the influence of Fe clusters and S doping on the activity centers of Fe-N and their impact on the ORR reaction, we developed four catalyst models, namely FeN₄-C, FeN₃S₁-C, Fe₄-FeN₄-C, Fe₄-FeN₃S₁-C, and heterojunction models combining OOH*, O*, and OH*. We evaluated the performance of these materials under applied dipole potential along the z-direction to account for electric field effects. All structures were optimized to achieve maximum stability. During the geometry optimization process, all atomic positions were allowed to relax. In this exercise, Brillouin zone sampling was conducted using Monkhorst–Pack (MP)⁶ grids of special points, with a separation of 0.04 Å⁻¹. The convergence criterion for the electronic self-consistent field (SCF) loop was set to 1 × 10⁻⁵ eV/atom. The atomic structures were optimized until the

residual forces reached a magnitude lower than $0.05 \text{ eV}\text{\AA}^{-1}$. The differential charge density was calculated using the following procedure:

$$\Delta\rho = \rho_{\text{tot}} - \rho_{\text{sub}} - \rho_{\text{abs}}, \quad (9)$$

where ρ_{tot} is the total charge density, and ρ_{sub} and ρ_{abs} represent the charge density of the substrate and absorbed molecules, respectively.

The free-energy change (ΔG) for adsorptions was calculated as follows:

$$\Delta G = E_{\text{total}} - E_{\text{slab}} - E_{\text{mol}} + \Delta E_{\text{ZPE}} - T\Delta S, \quad (10)$$

where E_{total} , E_{slab} , E_{mol} , ΔE_{ZPE} , and ΔS represent the total energy for the adsorption state, energy of the pure surface, energy of the adsorption molecule, zero-point energy change, and entropy change, respectively.

Molecular dynamics simulation: The molecular dynamics simulations were performed by using Gromacs 2021.6 package⁷⁻⁸ to reveal the nanostructures as well as the ionic conduction mechanism in CNF@PVA-SSE. General Amber force fields parameters⁹ and RESP charges^[10] were used for all molecules.¹¹ The force field parameters were obtained through Sob Top software.¹² To get the equilibrium structure of the mixed solution, NPT runs were performed at 298 K for 100 ns for each simulation system. Visualization of the structures is made by using VMD software.¹³

Reference

1. P. Giannozzi, S. Baroni, N. Bonini, M. Calandra, R. Car, C. Cavazzoni, D. Ceresoli, G. L. Chiarotti, M. Cococcioni, I. Dabo, A. Dal Corso, S. de Gironcoli, S. Fabris, G. Fratesi, R. Gebauer, U. Gerstmann, C. Gougoussis, A. Kokalj, M. Lazzeri, L. Martin-Samos, N. Marzari, F. Mauri, R. Mazzarello, S. Paolini, A. Pasquarello, L. Paulatto, C. Sbraccia, S. Scandolo, G. Sclauzero, A. P. Seitsonen, A. Smogunov, P. Umari and R. M., *J. Phys.: Condens. Matter.* 2009, **21**, 395502.
2. P. Giannozzi, O. Andreussi, T. Brumme, O. Bunau, M. Buongiorno Nardelli, M. Calandra, R. Car, C. Cavazzoni, D. Ceresoli, M. Cococcioni, N. Colonna, I. Carnimeo, A. Dal Corso, S. de Gironcoli, P. Delugas, R. A. DiStasio Jr, A. Ferretti, A. Floris, G. Fratesi, G. Fugallo, R. Gebauer, U. Gerstmann, F. Giustino, T. Gorni, J. Jia, M. Kawamura, H.-Y. Ko, A. Kokalj, E. Küçükbenli, M. Lazzeri, M. Marsili, N. Marzari, F. Mauri, N. L. Nguyen, H.-V. Nguyen, A. Otero-de-la-Roza, L. Paulatto, S. Poncé, D. Rocca, R. Sabatini, B. Santra, M. Schlipf, A. P. Seitsonen, A. Smogunov, I. Timrov, T. Thonhauser, P. Umari, N. Vast, X. Wu and S. Baroni, *J. Phys.: Condens. Matter.* 2017, **29**, 465901.
3. J. P. Perdew, K. Burke and M. Ernzerhof, *Phys. Rev. Lett.* 1996, **77 (18)**, 3865-3868.
4. P. E. Blöchl, O. Jepsen and O.K., *Phys. Rev. B.* 1994, **49 (23)**, 16223-16233.
5. G. Kresse and D. Joubert, *Phys. Rev. B.* 1999, **59 (3)**, 1758-1775.
6. H. J. Monkhorst and J. D., *Phys. Rev. B.* 1976, **13 (12)**, 5188-5192.
7. Abraham, M. J.; Murtola, T.; Schulz, R.; Páll, S.; Smith, J. C.; Hess, B.; Lindahl, E. GROMACS: High Performance Molecular Simulations through Multi-Level Parallelism from Laptops to Supercomputers. *SoftwareX.* **2015**, **1–2**, 19–25.
8. Van Der Spoel, D.; Lindahl, E.; Hess, B.; Groenhof, G.; Mark, A. E.; Berendsen, H. J. C. GROMACS: Fast, Flexible, and Free. *J. Comput. Chem.* **2005**, **26**, 1701–1718.
9. Wang J.; Wang, W.; Kollman P. A.; Case, D. A. Automatic atom type and bond type perception in molecular mechanical calculations. *J. Mol. Graph. Model.* **2006**, **25**, 247.
10. Cieplak, P.; Cornell, W. D.; Bayly, C.; Kollman, P. A. Application of the

- multimolecule and multiconformational RESP methodology to biopolymers: Charge derivation for DNA, RNA, and proteins. *J. Comput. Chem.*, **1995**, **16**, 1357–1377.
11. Bayly, C.; Cornell, W. D.; Kollman, P. A. A well-behaved electrostatic potential based method using charge restraints for deriving atomic charges: the RESP model. *J. Phys. Chem.*, **1993**, **97**, 10269–10280.
12. Lu, T., Sobtop, Version 1.0, <http://sobereva.com/soft/Sobtop> (accessed on 12/01/2022)
13. Humphrey, W.; Dalke, A.; Schulten, K. VMD: Visual Molecular Dynamics. *J. Mol. Graphics*. **1996**, **14**, 33–38

S2. Supplementary Figures and Tables

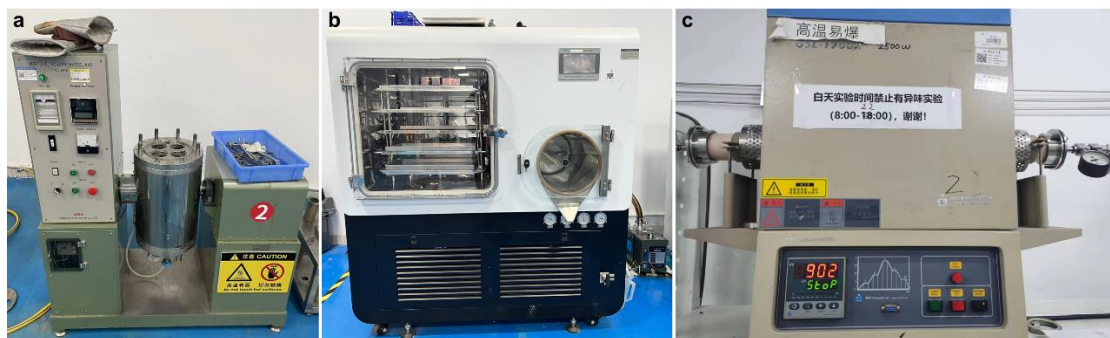


Fig. S1 The process for scaling up the synthesis of single-atom catalysts obtained from pulping black liquor involved the following steps: (a) Preparation of black liquor in a 4 L reactor through batch processing; b) Freeze-drying of precursors derived from Fe-rich neutral black liquors using a pilot-type lyophilizer; (c) Efficient production of SACs derived from black liquor for paper manufacturing was achieved using high-capacity tube furnaces.

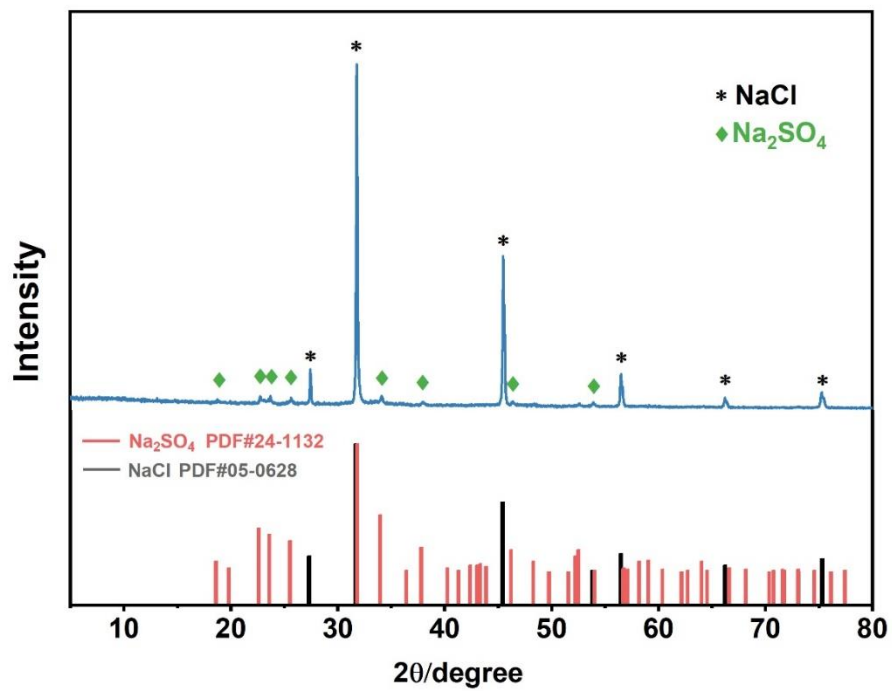


Fig. S2 (a) XRD of Fe_2O_3 -SC before water washing;

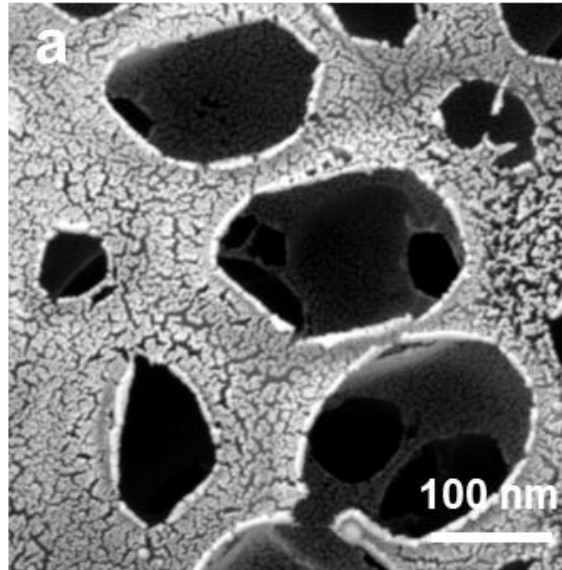


Fig.S3 (a) Surface enlargement of Fe_x/FeN₃S₁-C.

Fig. S3 presents an enlarged view of Fe_x/FeN₃S₁-C, where many wormlike cracks are evenly distributed throughout the carbon substrate surface, suggesting that the development of a hierarchical pore structure is aided by the synergistic action of NaCl and Na₂SO₃.

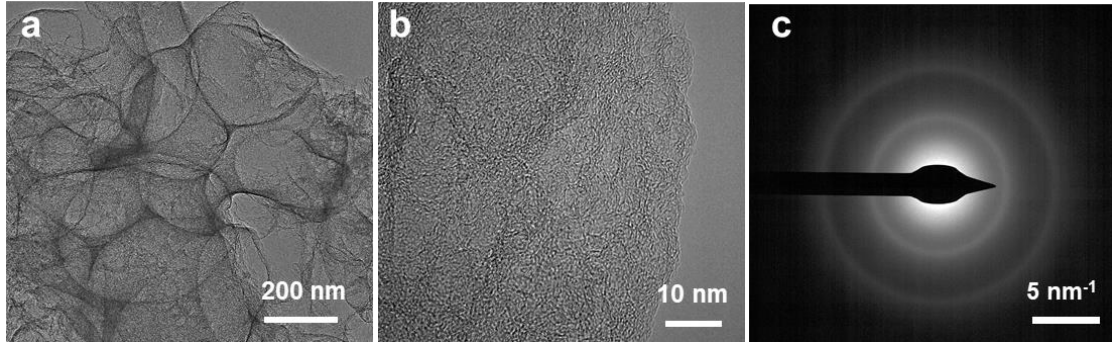


Fig. S4 (a-b) TEM and High magnification TEM and c) SAED of images $\text{Fe}_x/\text{FeN}_3\text{S}_1$ -

C.

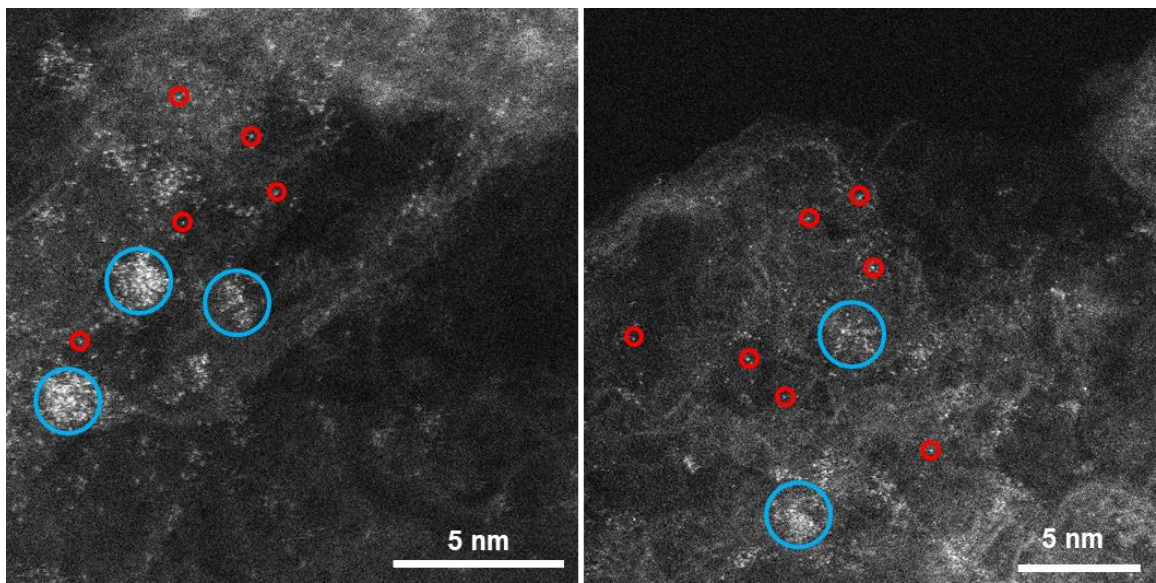


Fig. S5 Spherical Aberration Corrected Transmission Electron Microscope (AC-TEM) image showing highly dispersed Fe atoms in carbon layers. Single Fe atoms highlighted by red circles; Fe clusters highlighted by blue circles.

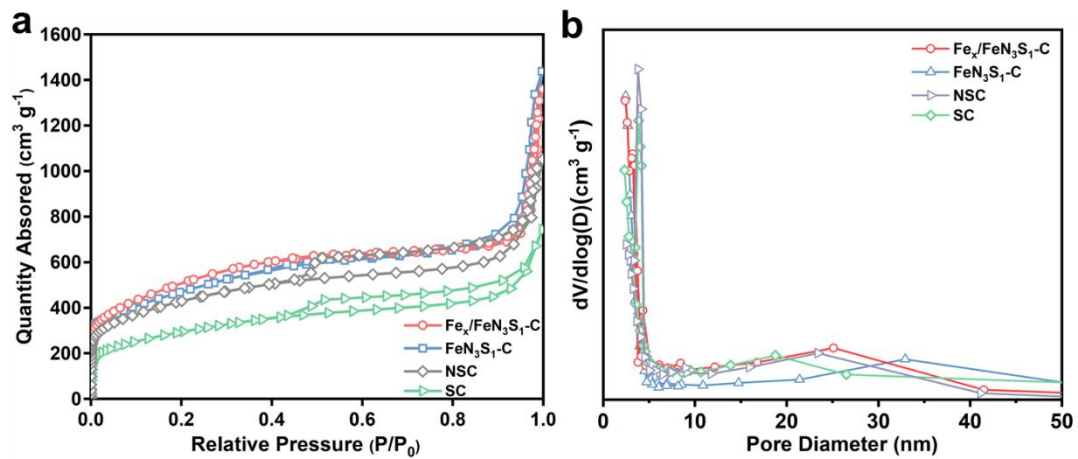


Fig. S6. (a) N_2 adsorption/desorption isotherms; (b) pore size distributions of Fe_x/FeN_3S_1-C , FeN_3S_1-C , NSC and SC;

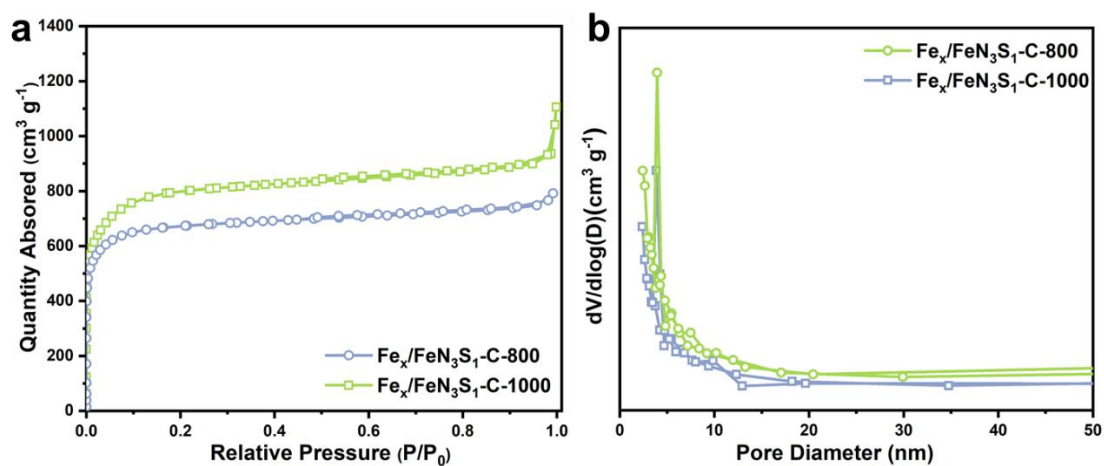


Fig. S7. (a) N_2 adsorption/desorption isotherms; (b) pore size distributions of $Fe_x/FeN_3S_1-C-800$ and $Fe_x/FeN_3S_1-C-1000$.

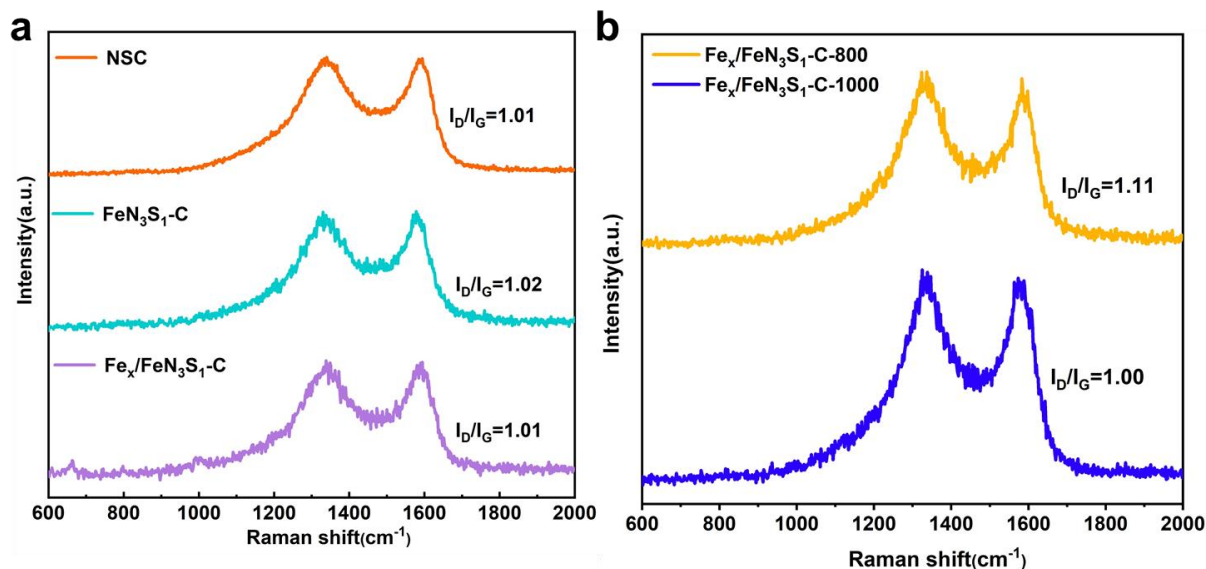


Fig. S8 Raman spectrum of (a) $\text{Fe}_x/\text{FeN}_3\text{S}_1\text{-C}$, $\text{FeN}_3\text{S}_1\text{-C}$, NSC and (b) $\text{Fe}_x/\text{FeN}_3\text{S}_1\text{-C-800}$ and $\text{Fe}_x/\text{FeN}_3\text{S}_1\text{-C-1000}$.

The Raman spectra of all the samples in Fig. S8 show two peaks at 1340 cm^{-1} and 1605 cm^{-1} which could be ascribed to the D band (defective/disordered carbon) and G band (graphitic carbon) of carbon species. No distinct difference in the intensity ratio of D band and G band (I_D/I_G) is observed among these catalysts, indicating their similar degree of graphitization. These results demonstrate that the Fe-doping and acid etching did not strongly affect the structural disorder of carbon framework. In particular, the $\text{Fe}_x/\text{FeN}_3\text{S}_1\text{-C}$ possesses a high I_D/I_G ratio (1.01), which suggests a disordered and defective carbon matrix, offering sufficient channels for oxygen adsorption and intermediate product (OOH^* and OH^*) transportation so as to further improve the ORR.

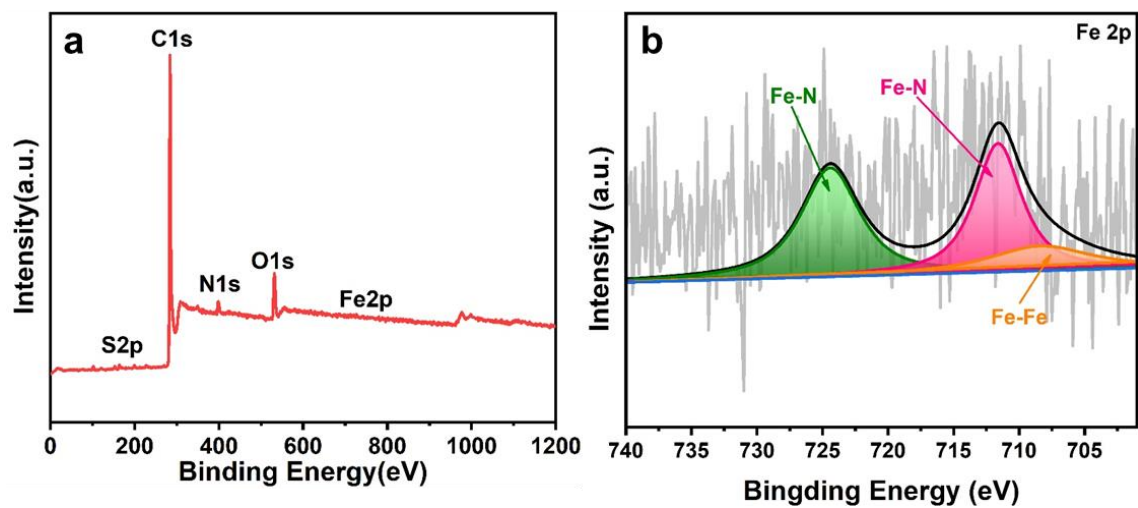


Fig. S9 (a) XPS survey spectrum of $\text{Fe}_x/\text{FeN}_3\text{S}_1\text{-C}$. (b) High-resolution Fe 2p spectrum of $\text{Fe}_x/\text{FeN}_3\text{S}_1\text{-C}$ catalyst.

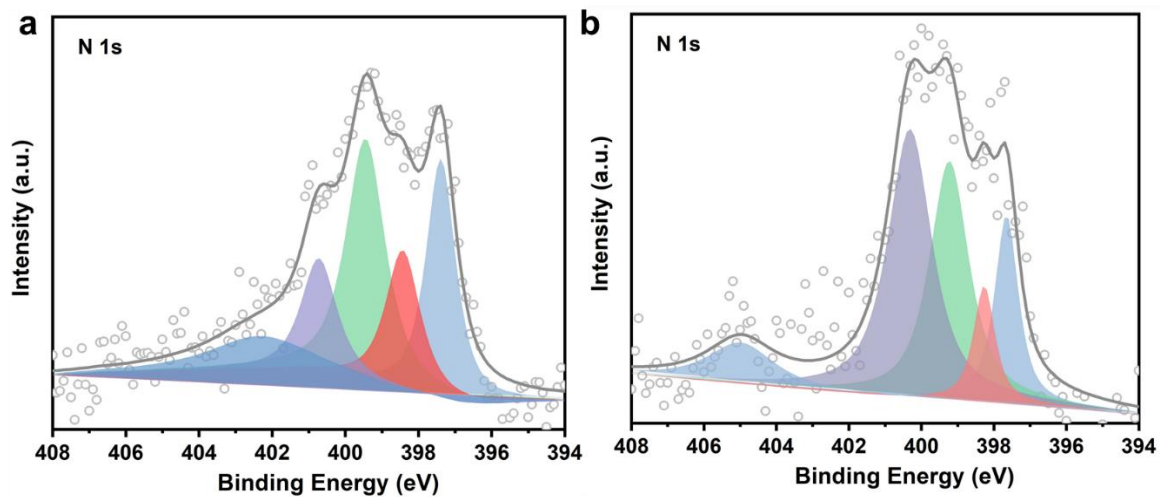


Fig. S10 (a) High-resolution N1S spectrum of $\text{Fe}_x/\text{FeN}_3\text{S}_1\text{-C-800}$ and $\text{Fe}_x/\text{FeN}_3\text{S}_1\text{-C-1000}$ catalyst.

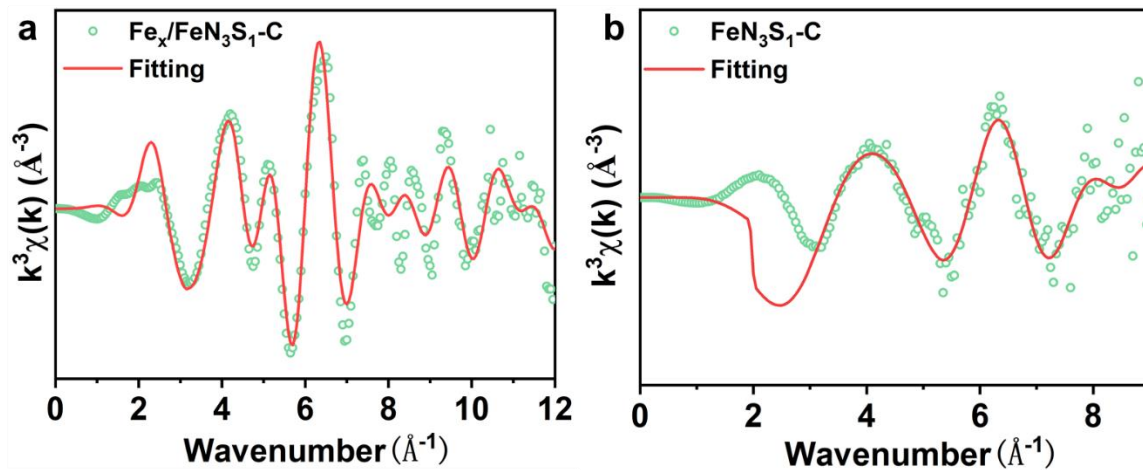


Fig. S11 (a, b) Fe K-edge EXAFS fitting curves in k space for $\text{Fe}_x/\text{FeN}_3\text{S}_1\text{-C}$ and $\text{FeN}_3\text{S}_1\text{-C}$.

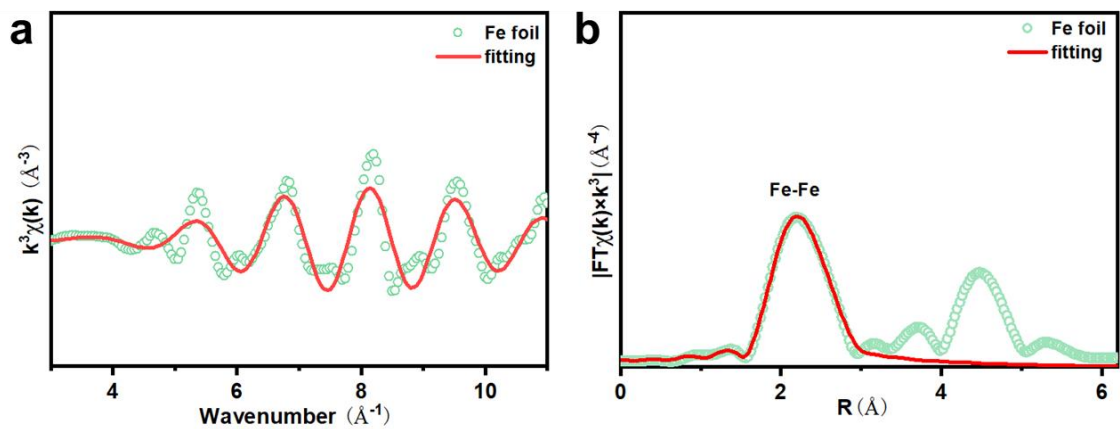


Fig. S12 FT of the Fe K-edge EXAFS spectra in (a) k and b) R space and the corresponding fitting curves for Fe foil.

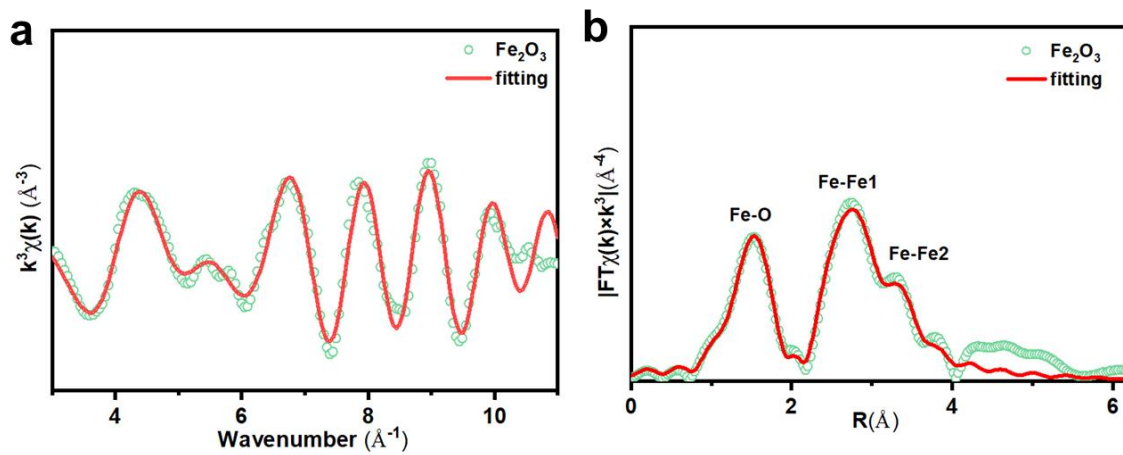


Fig. S13 FT of the Fe K-edge EXAFS spectra in (a) k and b) R space and the corresponding fitting curves for Fe₂O₃.

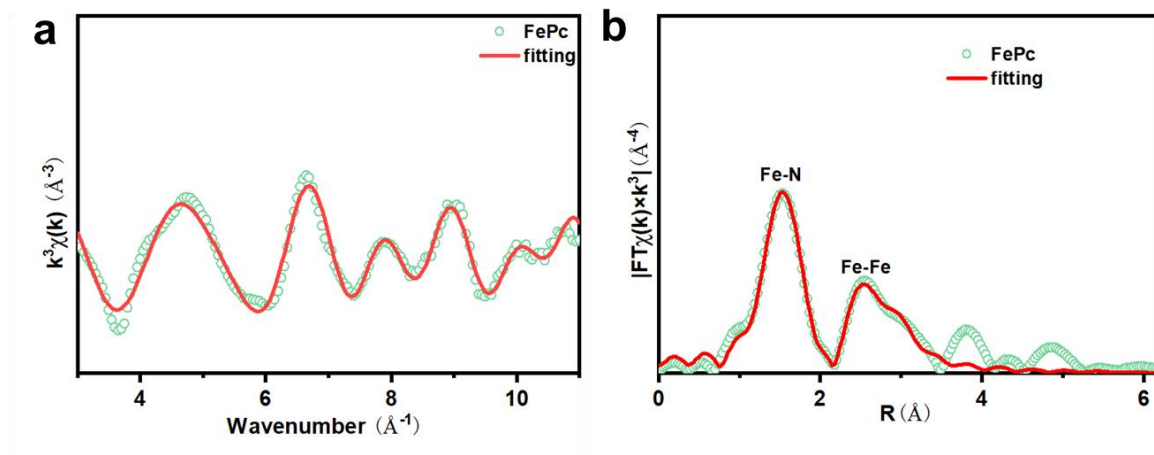


Fig. S14 FT of the Fe K-edge EXAFS spectra in (a) k and b) R space and the corresponding fitting curves for FePc.

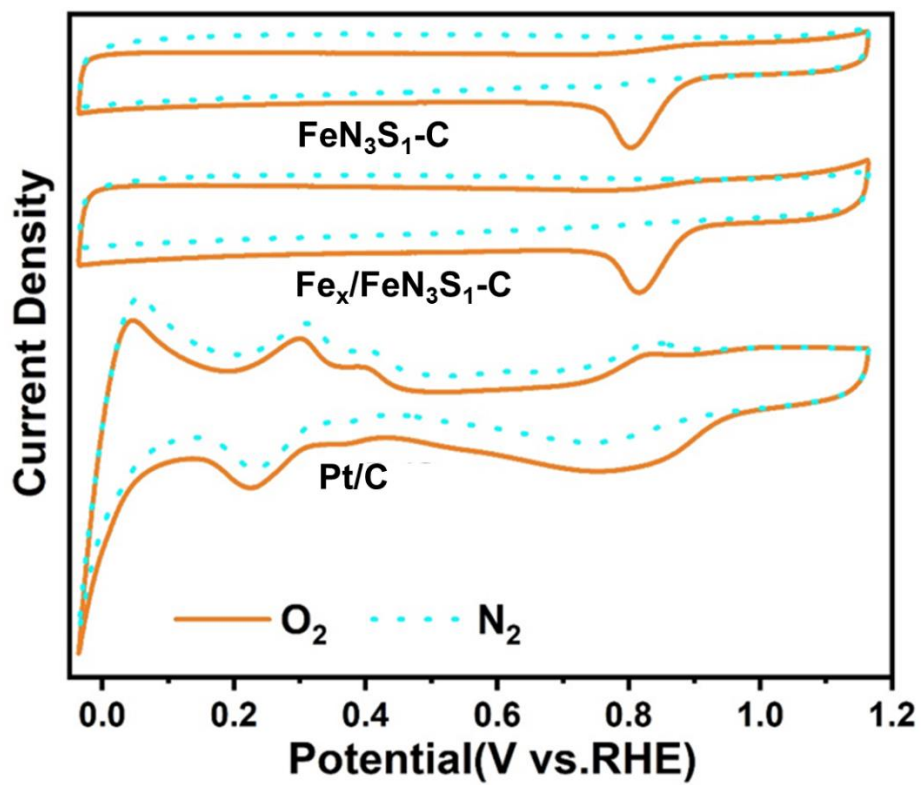


Fig. S15 CV curves of $\text{Fe}_x/\text{FeN}_3\text{S}_1\text{-C}$ and Pt/C in O_2 or N_2 saturated 0.1 M KOH solution.

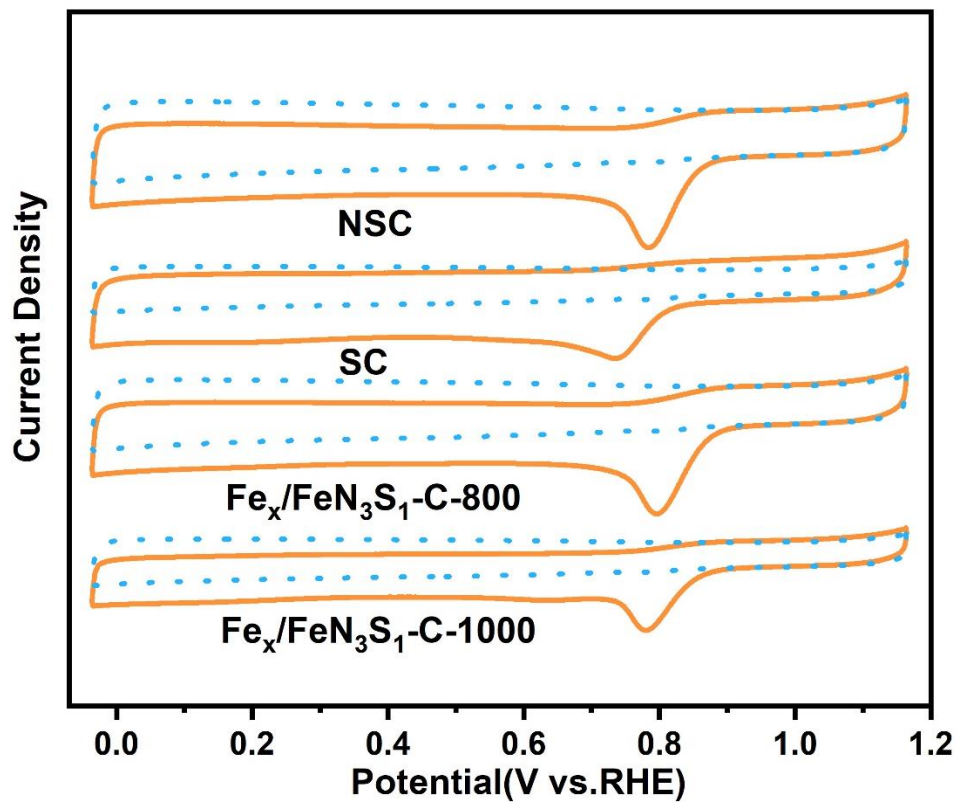


Fig. S16 CV curves of NSC, SC, Fe_x/FeN₃S₁-C-800 and Fe_x/FeN₃S₁-C-800 in O₂ or N₂ saturated 0.1 M KOH solution.

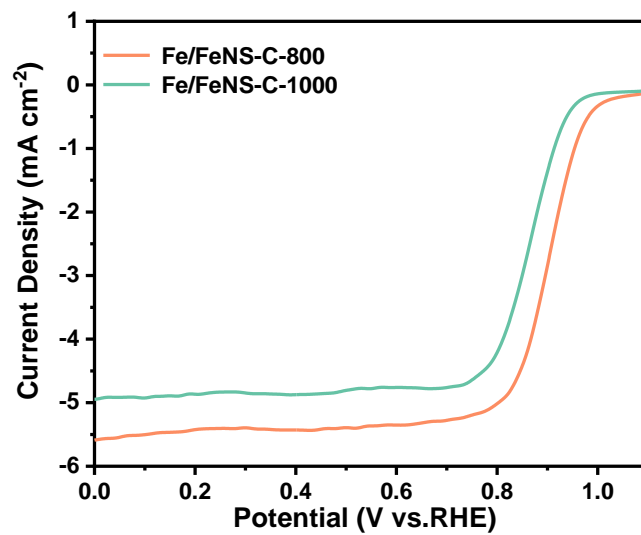


Fig. S17 The LSV curves of Fe_x/FeN₃S₁-C-800 and Fe_x/FeN₃S₁-C-1000.

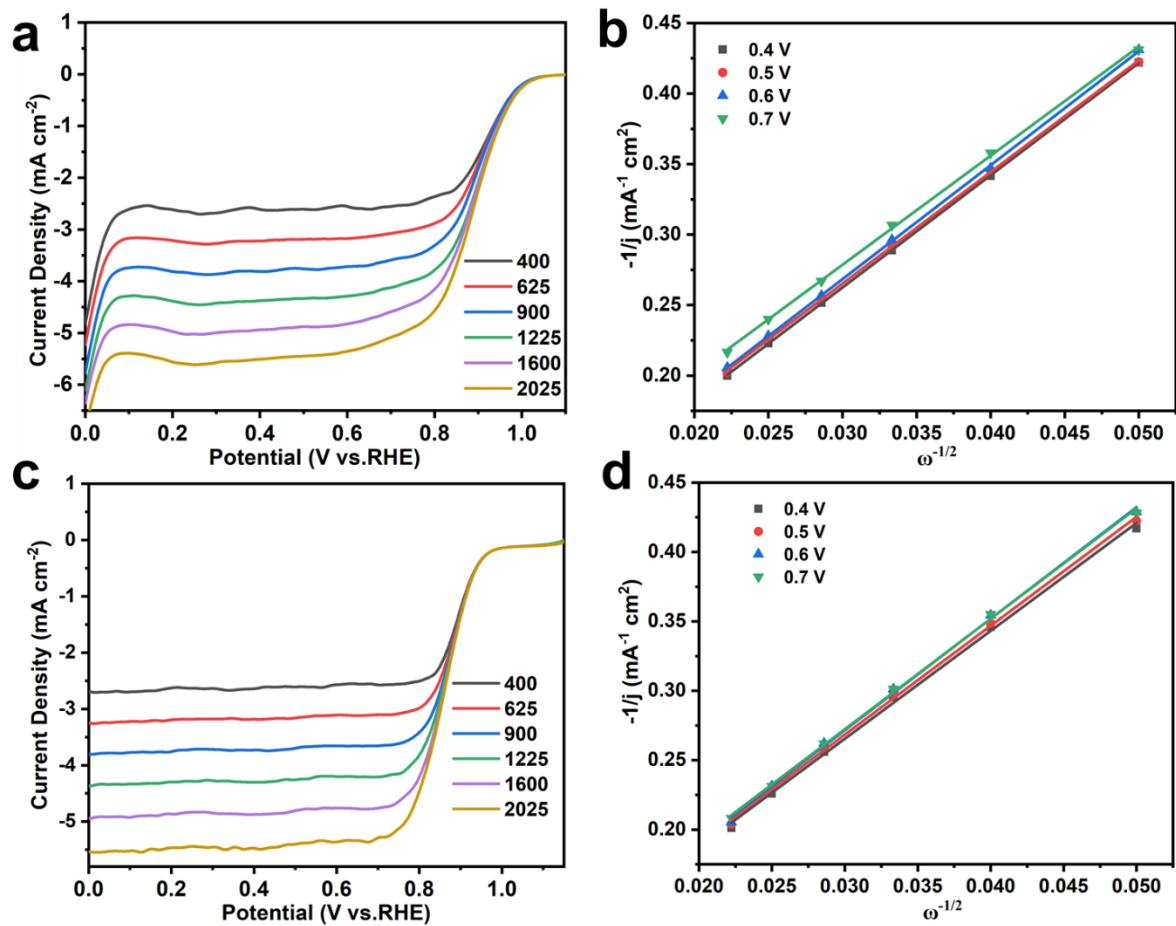


Fig. S18 The LSV curves of Pt/C (a) and FeN₃S₁-C (c) at different rotation rates and (b), (d) is the corresponding K-L curves of the catalyst.

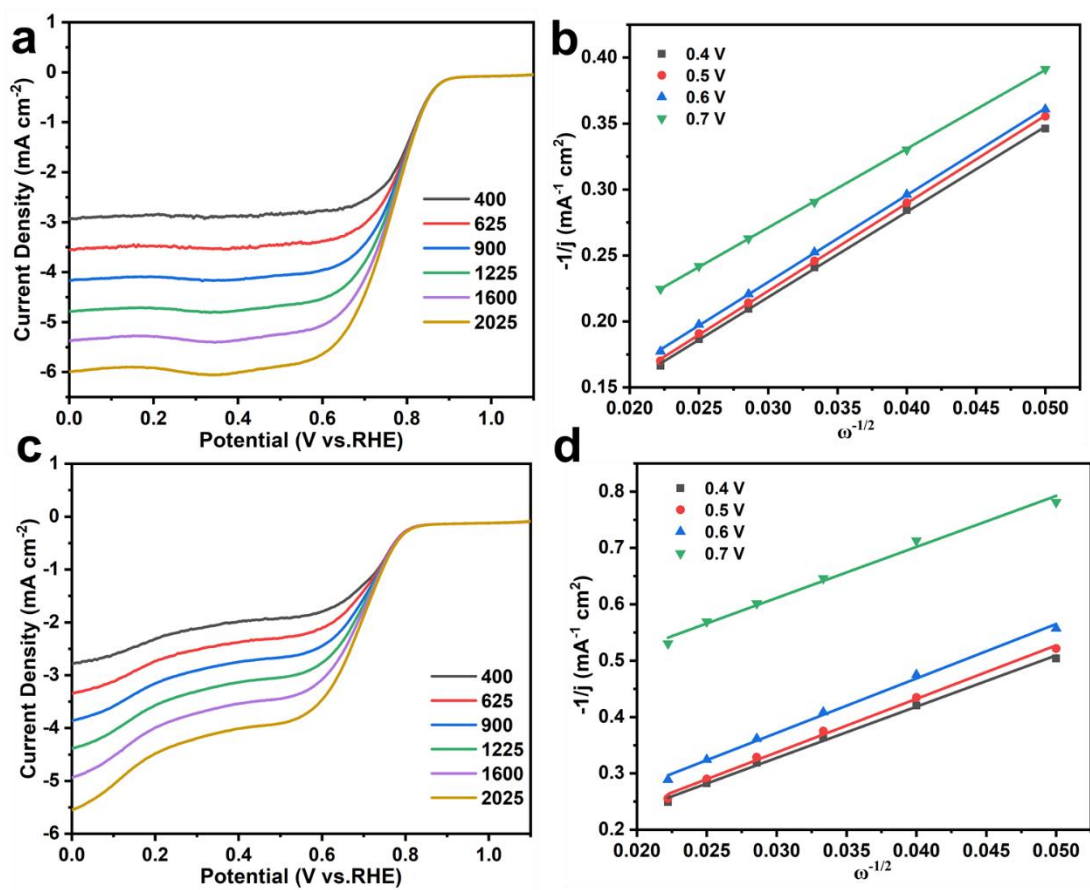


Fig. S19 The LSV curves of NSC (a) and SC (c) at different rotation rates and (b), (d) is the corresponding K-L curves of the catalyst.

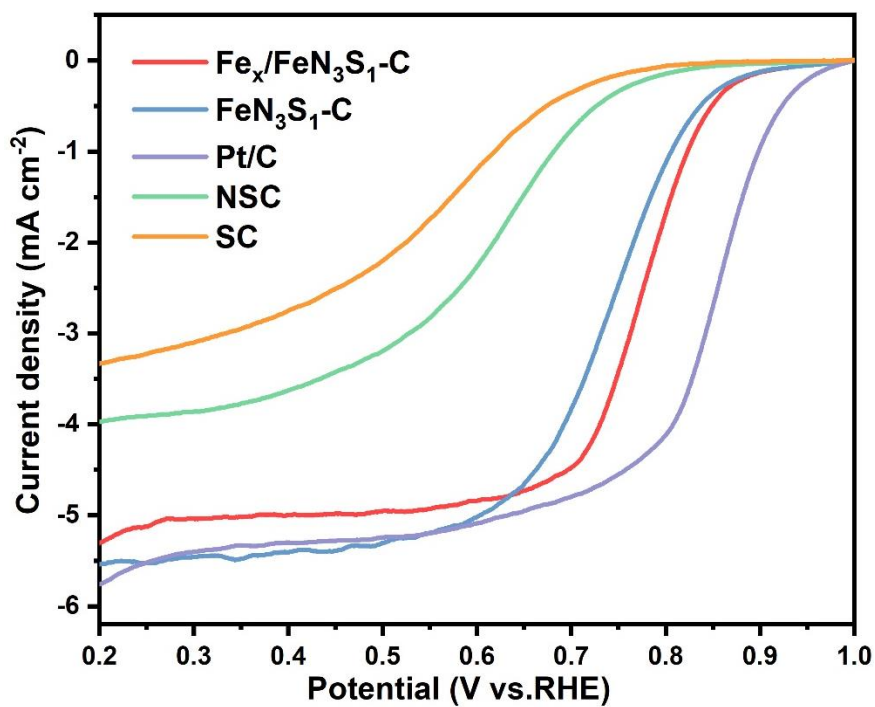


Fig. S20 ORR polarization curves of the samples in 0.1 M HClO₄.

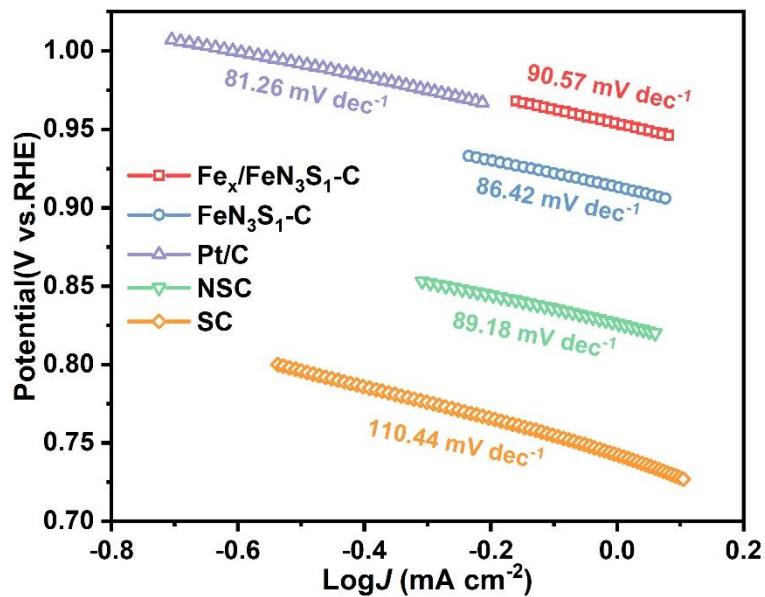


Fig. S21 Tafel plots of Fe_x/FeN₃S₁-C, FeN₃S₁-C, Pt/C, NSC and SC.

The Tafel slope of Fe_x/FeN₃S₁-C is measured at 90.57 mV dec⁻¹, surpassing that of FeN₃S₁-C (86.42 mV dec⁻¹), Pt/C (81.26 mV dec⁻¹), and NSC (89.18 mV dec⁻¹), indicating the rapid ORR kinetics achieved by Fe_x/FeN₃S₁-C, as shown in Fig. S21.

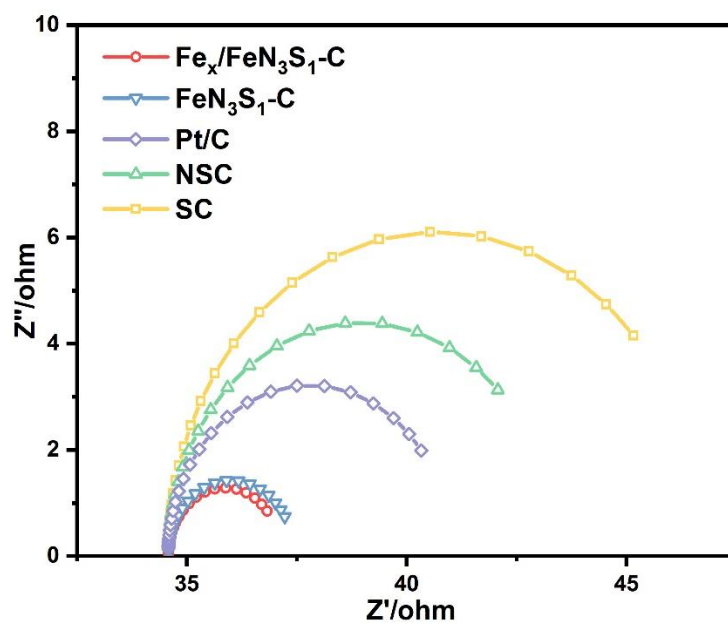


Fig. S22 The Nyquist plots of all samples.

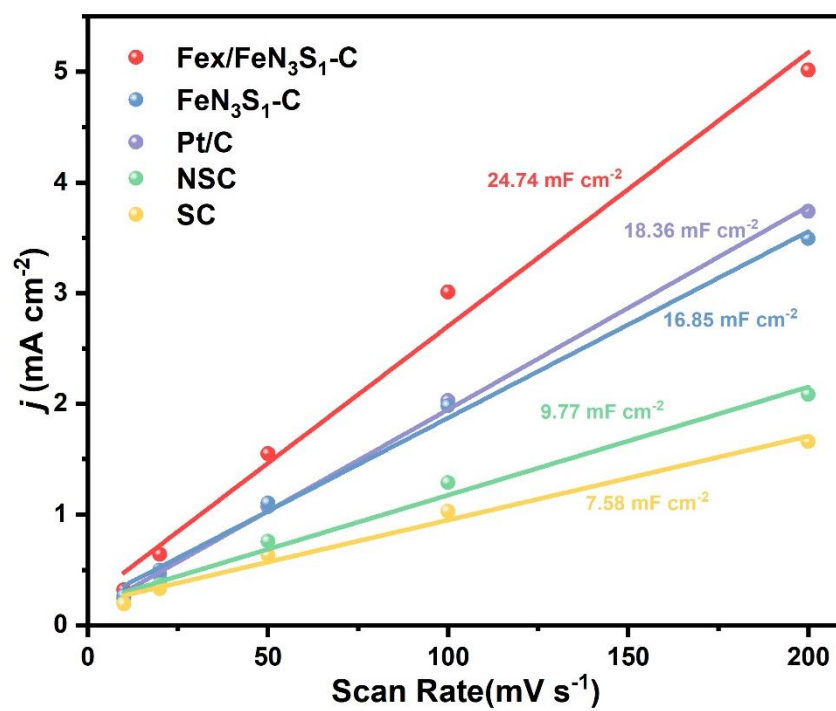


Fig. S23 Cdl of all samples.

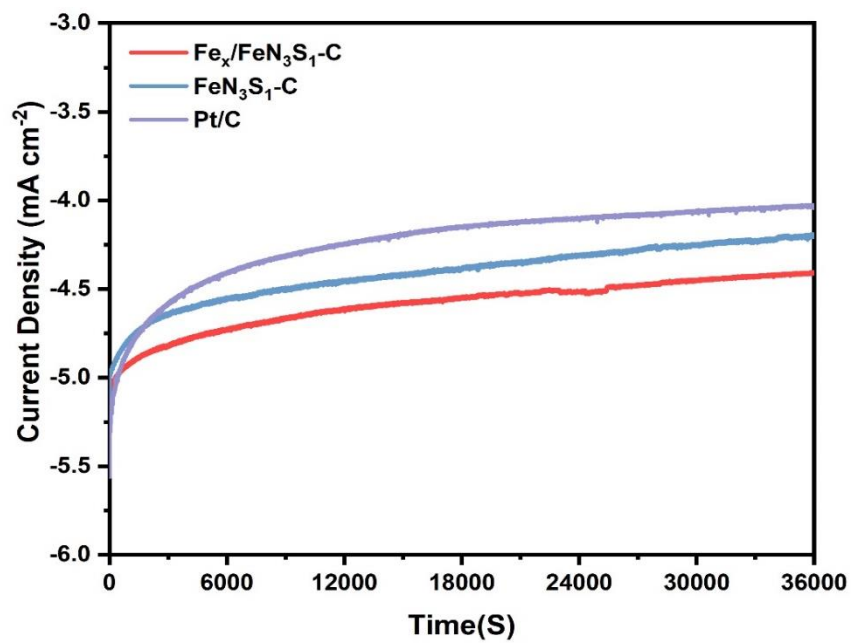


Fig. S24 Stability tests of Fe_x/FeN₃S₁-C, FeN₃S₁-C, Pt/C for ORR at -0.4 V.

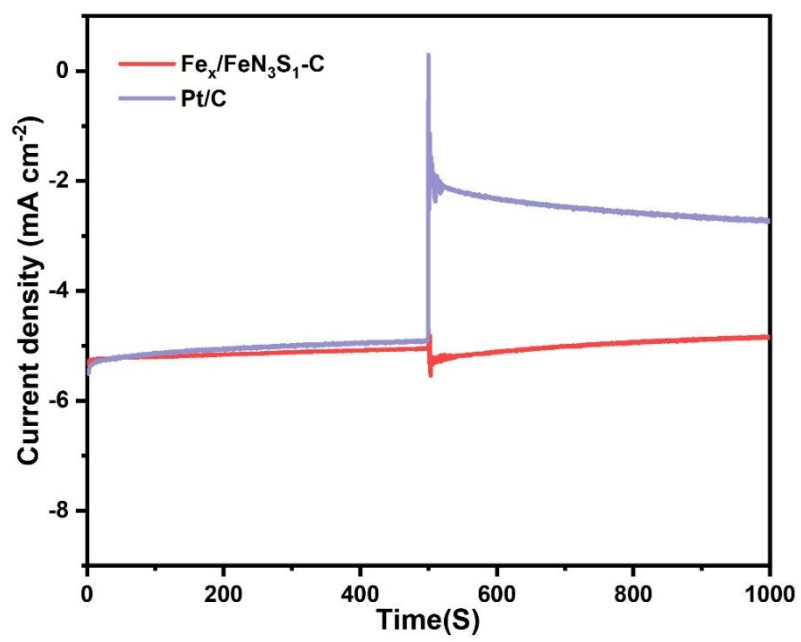


Fig. S25 Methanol tolerance measurements of Fe_x/FeN₃S₁-C and commercial Pt/C at the same condition, and the addition of methanol was immitted after 500 s.

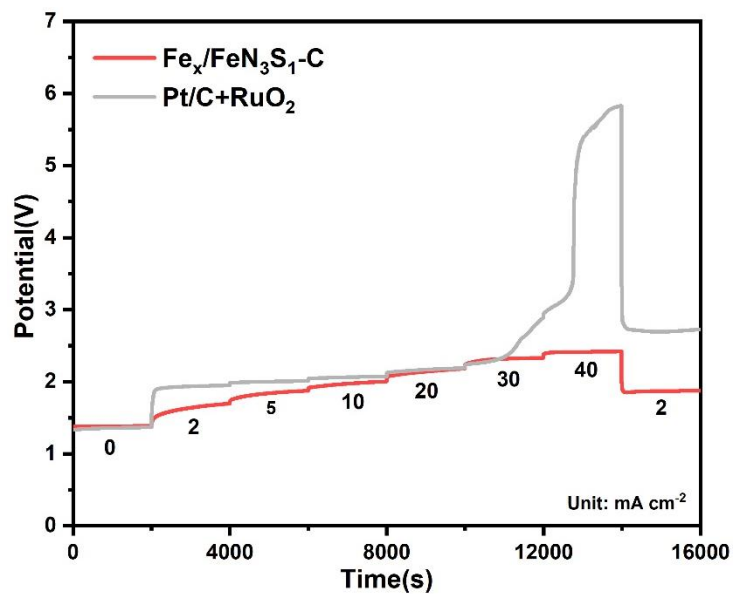


Fig. S26. Charge curves of Fe_x/FeN₃S₁-C -ZABs and Pt/C+RuO₂-ZABs at different current densities;

As shown in Fig. S26, the charging voltage of Fe_x/FeN₃S₁-C-ZABs continuously lower than Pt/C+RuO₂-ZABs with increasing current density, implied that Fe_x/FeN₃S₁-C reduces the charging voltage of ZABs and could remain stable at high current density.

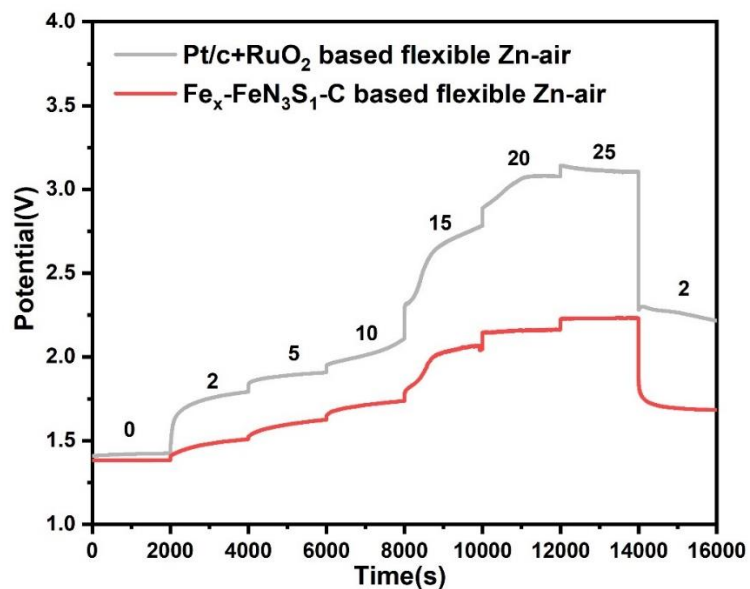


Fig. S27 Charge curves of Fe_x/FeN₃S₁-C based flexible ZABs and Pt/C+RuO₂ based flexible ZABs at different current densities;

Also, we performed multiplier charging tests on flexible batteries, Fe_x/FeN₃S₁-C assembled flexible batteries maintain a low charging voltage than Pt/c+RuO₂ based flexible Zn-air battery throughout the charging process and can withstand high-current charging

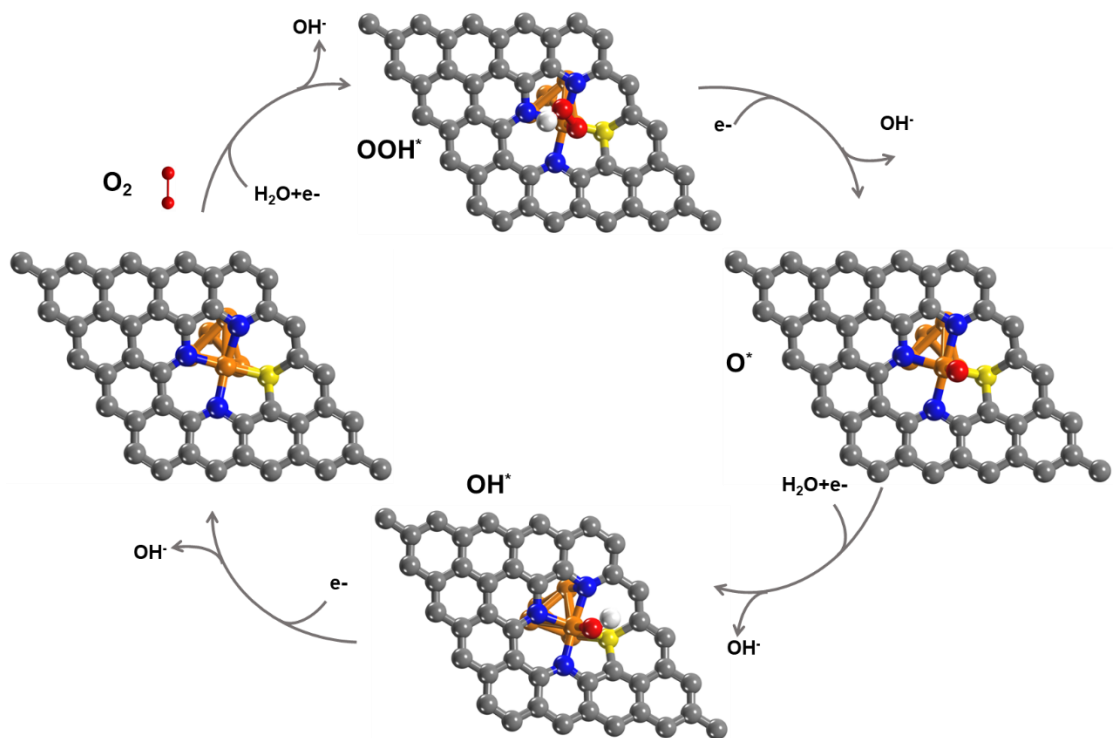


Fig. S28 ORR mechanism in alkaline solution of Fe₄-FeN₃S₁-C structure. Gray, red, white, yellow and orange balls represent C, O, H, S and Fe atoms, respectively (top view).

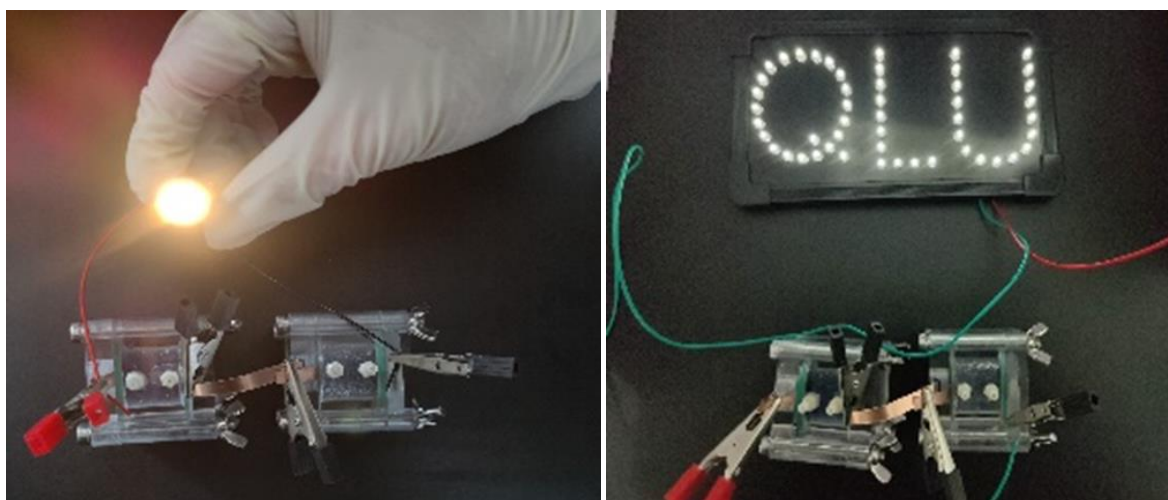


Fig. S29 Images of the LEDs powered by two Fe_x/FeN₃S₁-C-ZABs in series.

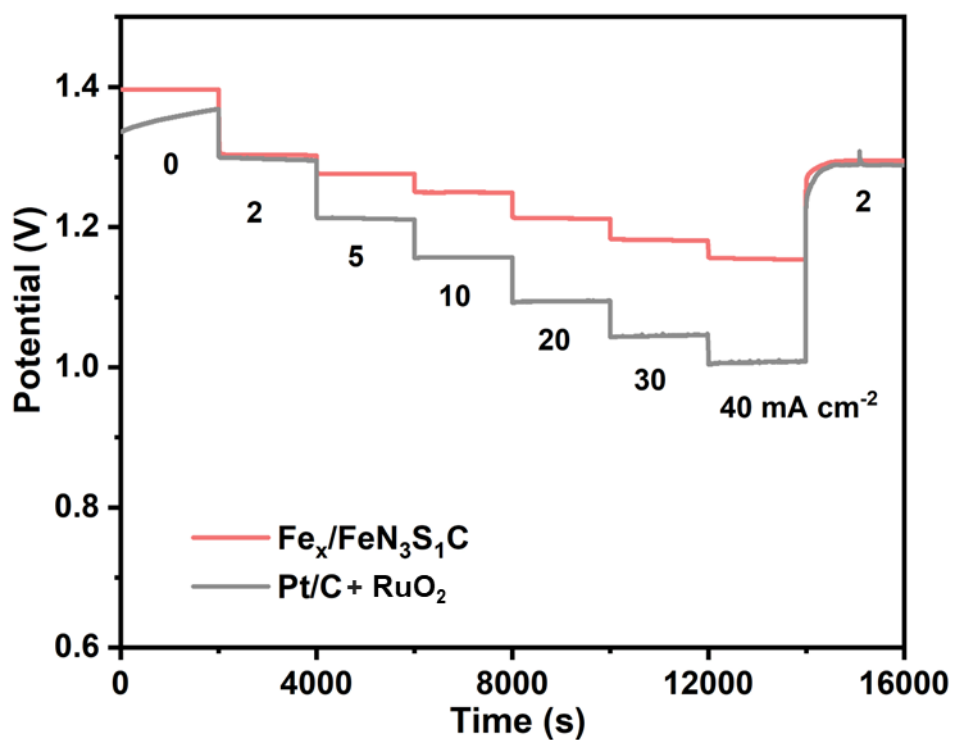


Fig. S30 Discharge curves of $\text{Fe}_x/\text{FeN}_3\text{S}_1\text{C}$ -ZABs and $\text{Pt/C} + \text{RuO}_2$ -ZABs at different current densities;

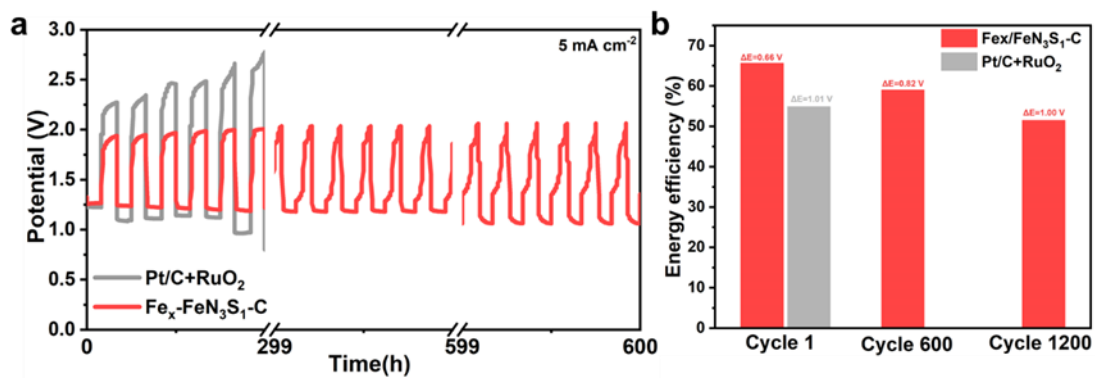


Fig. S31 (a) Galvanostatic discharge/charge curves of Fe_x/FeN₃S₁-C and Pt/C+ RuO₂ based batteries at 0-1 h (cycle1-cycle6), 299-300 h (cycle1794-cycle1800) and 599-600 h (cycle3594-cycle3600), respectively. (b) the energy utilization efficiency of Fe_x/FeN₃S₁-C and Pt/C+RuO₂ based batteries under different cycles.

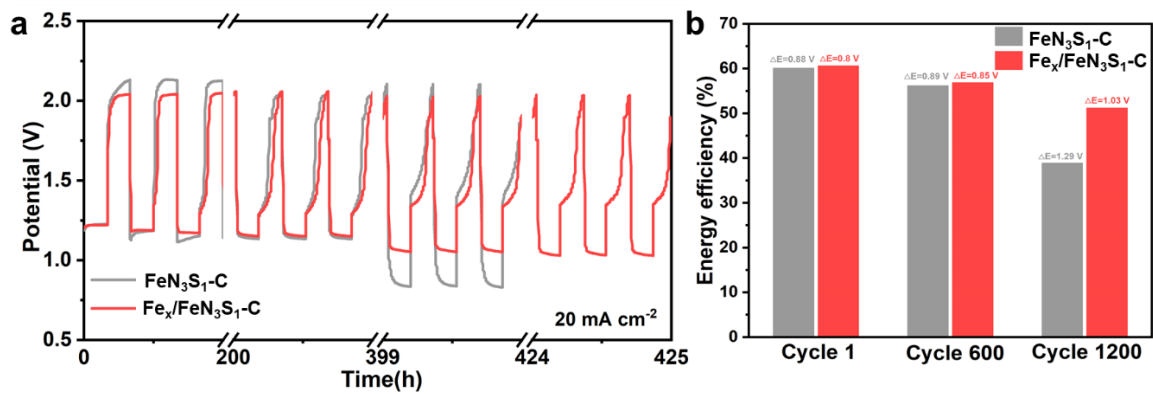


Fig. S32 (a) Galvanostatic discharge/charge curves of Fe_x/FeN₃S₁-C and FeN₃S₁-C based batteries at 0-1 h (cycle1-cycle3), 200-201 h (cycle600-cycle603), 399-400 h (cycle1200-cycle1203) and 424-425 h (cycle1272- cycle1275), respectively. (b) the energy utilization efficiency of Fe_x/FeN₃S₁-C and FeN₃S₁-C based batteries under different cycles.

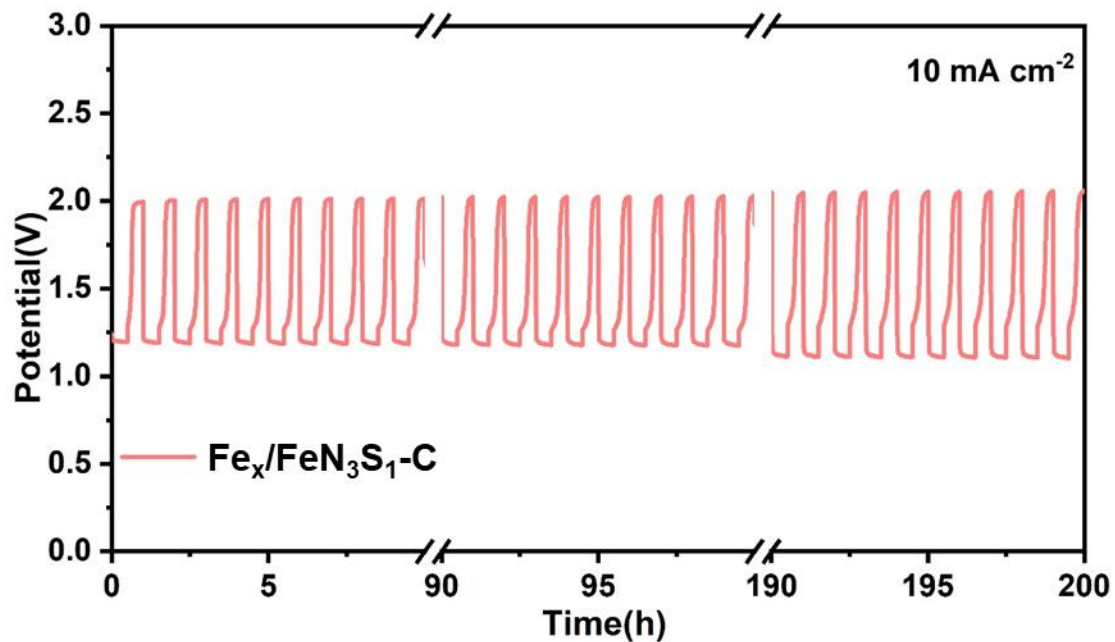


Fig. S33 Galvanostatic discharge/charge curves of Fe_x/FeN₃S₁-C at 10 mA cm⁻² for 1 h/cycle.

A longer cycle life test (10 mA cm⁻², 60 min/cycle) was conducted to evaluate the durability of Fe_x/FeN₃S₁-C-ZAB. As depicted in Fig. S33, Fe_x/FeN₃S₁-C-ZABs possessed an excellent round trip efficiency of 60.30% at the initial phase, which mildly attenuated to 54.14% after 200 h of galvanostatic discharge–charge cycling.

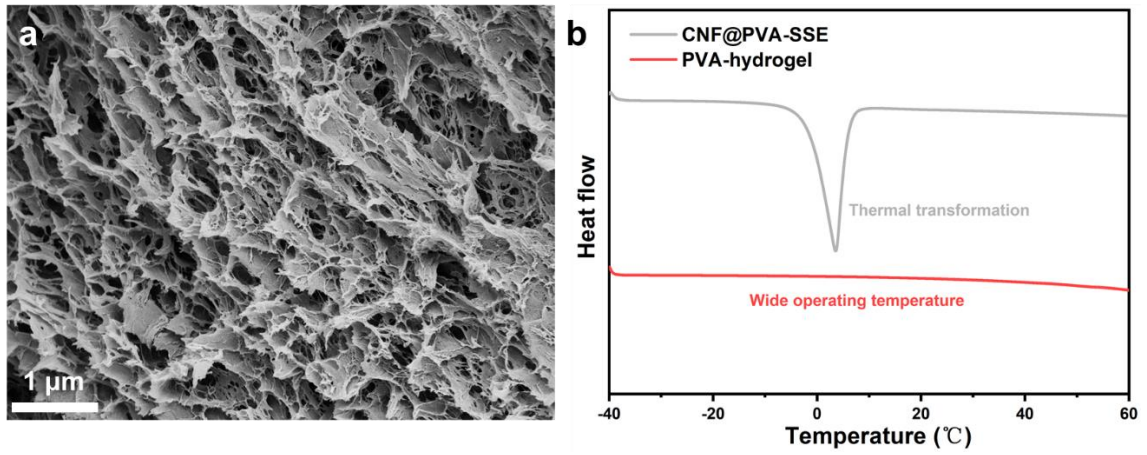


Fig. S34 (a) Photograph of the CNF@PVA-SSE; (b) Differential scanning calorimetric thermograms

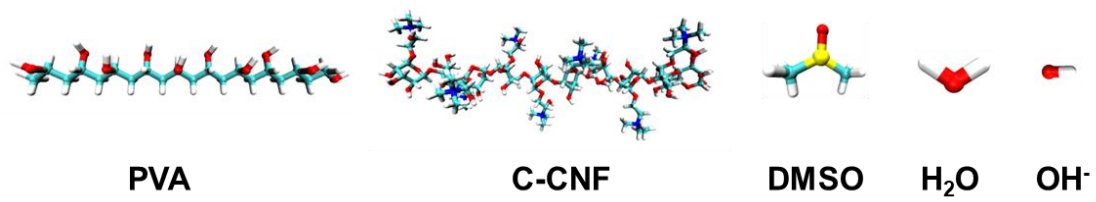


Fig. S35 Initial structural unit illustrated of Fig.6 a1-a4

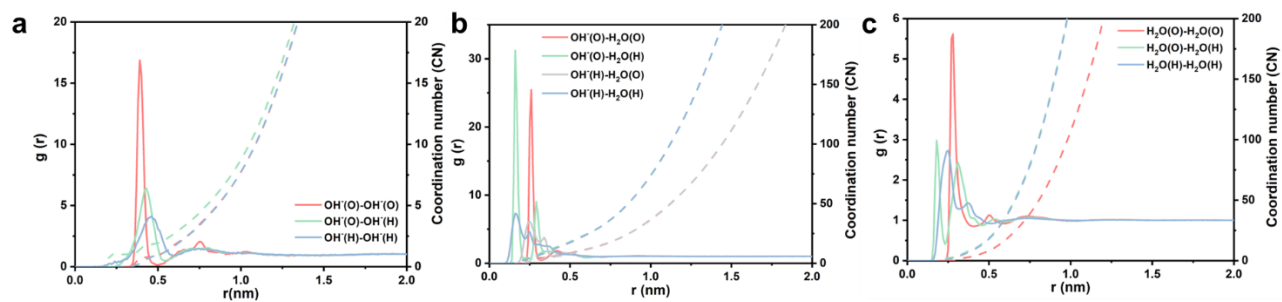


Fig. S36 Radial distribution function (RDF) and coordination number (CN): (a) OH^- – OH^- ; (b), OH^- – H_2O ; (c) H_2O – H_2O ;

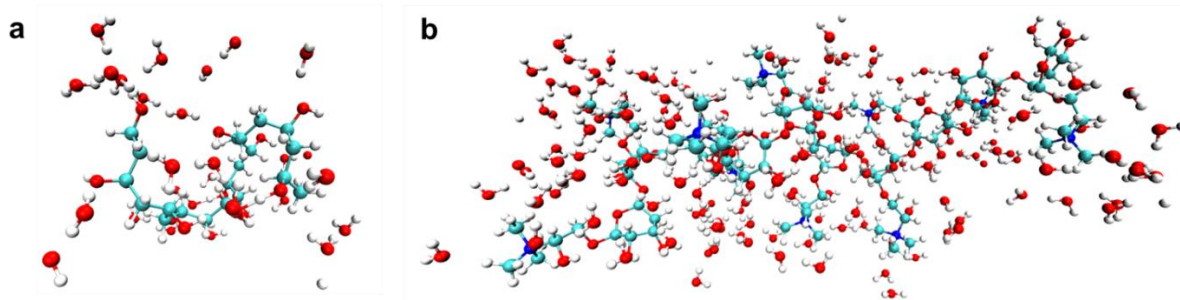


Fig. S37 (a) Hydrated structure of single PVA polymer chain and (b) Nanocellulose modified by quaternary ammonium salt chain

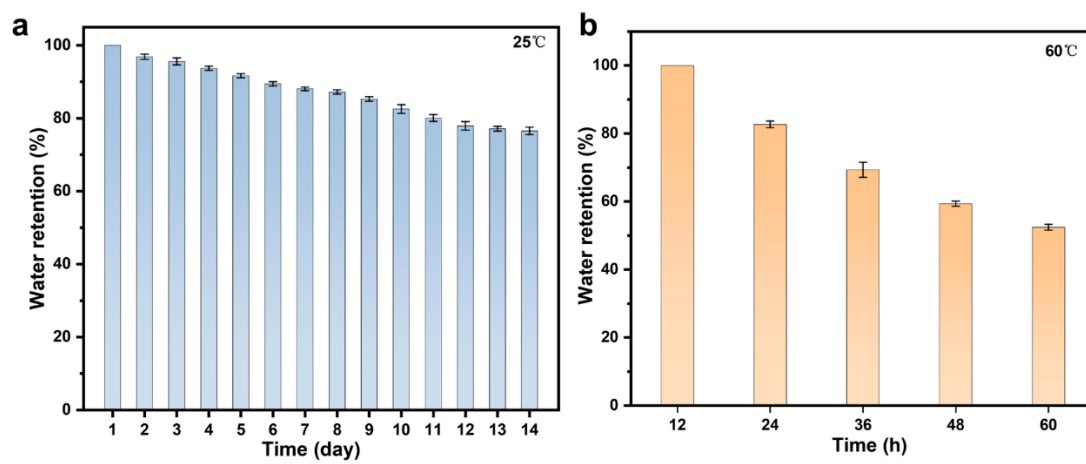


Fig. S38 Water retention capabilities of the CNF@PVA organhydrogel electrolyte at 25°C (a) and 60°C (b)

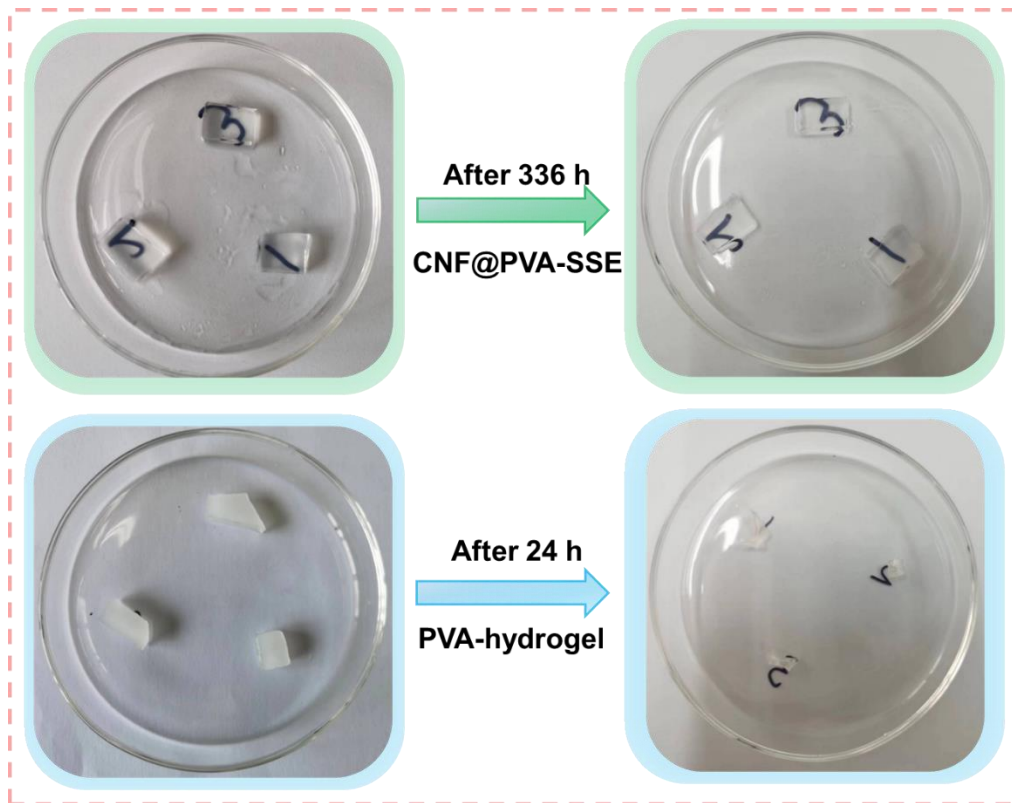


Fig. S39 Photographs of organhydrogel electrolytes after exposure at room temperature.

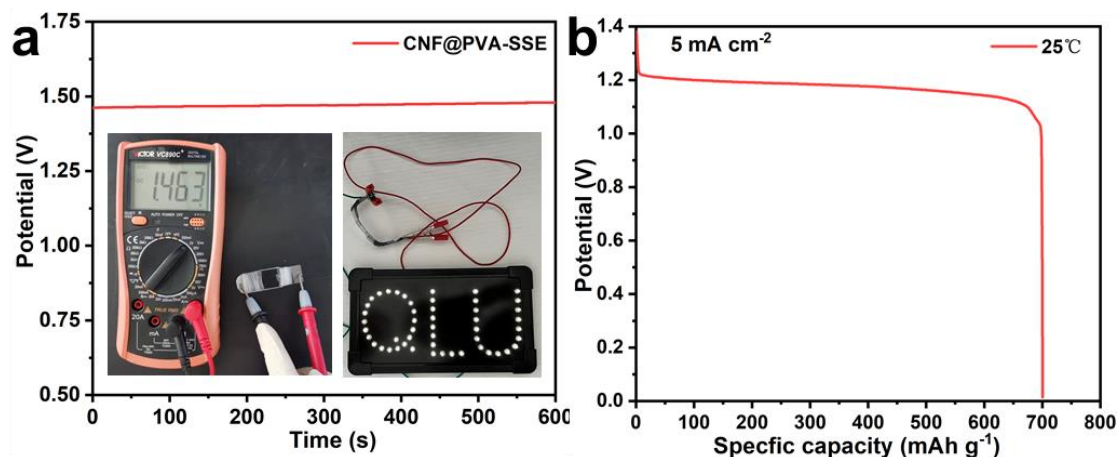


Fig. S40 (a) The open-circuit voltage of Wood-WTF-ZABs (the left insert shows the open-circuit voltage of a flexible Zn-air battery; and the right insert exhibits an LEDs powered by two Wood-WTF-ZABs in bending; (b) Galvanostatic discharge curves of Wood-WTF-ZABs at 5 mA cm⁻²;

The open circuit voltage of Wood-WTF-ZABs could reach 1.46 V and two batteries in series could power LEDs (~ 3V) at bending, suggesting an admirable performance as a flexible battery (Fig. S40a).

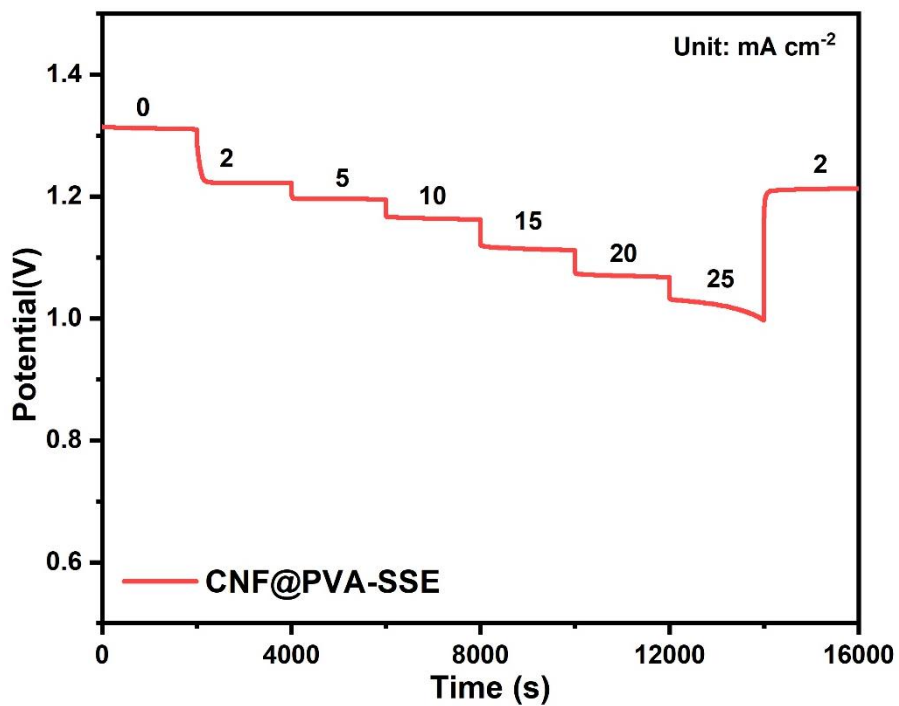


Fig. S41 Discharge curves of Wood-WTF-ZABs at different current densities.

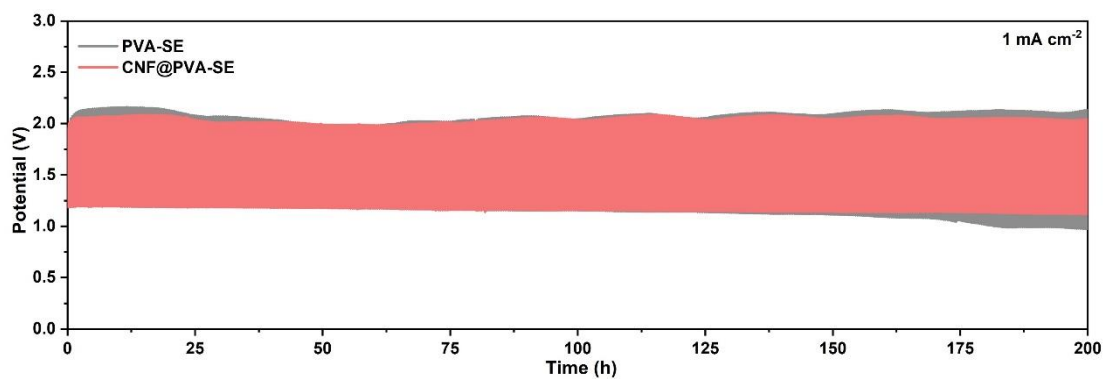


Fig. S42 Galvanostatic discharge/charge cycling curves of Wood-WTF-ZABs at 1 mA cm⁻² and 20 min/cycle

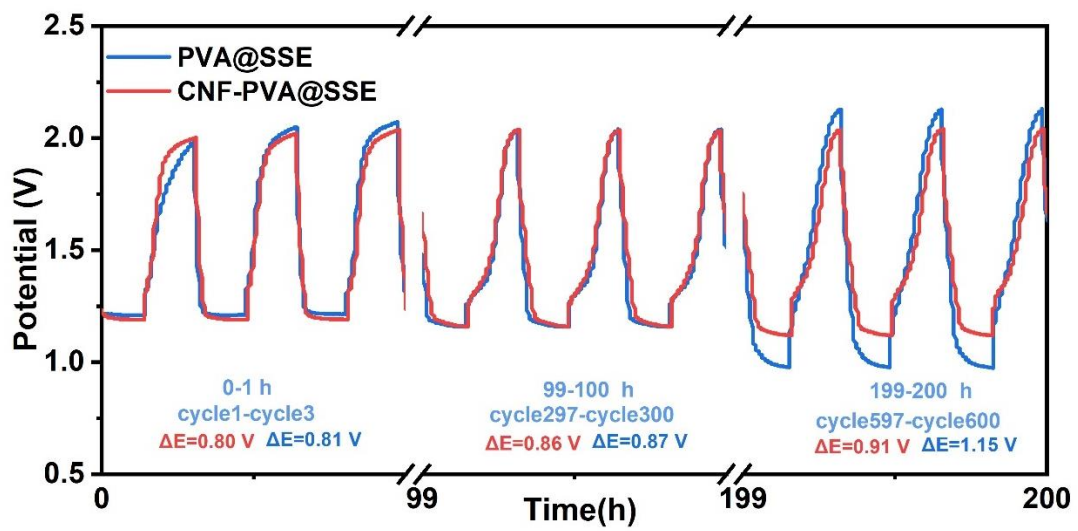


Fig. S43 Galvanostatic discharge/charge curves of Wood-WTF-ZABs at 0-1 h, 99-100 h and 199-200 h, respectively.

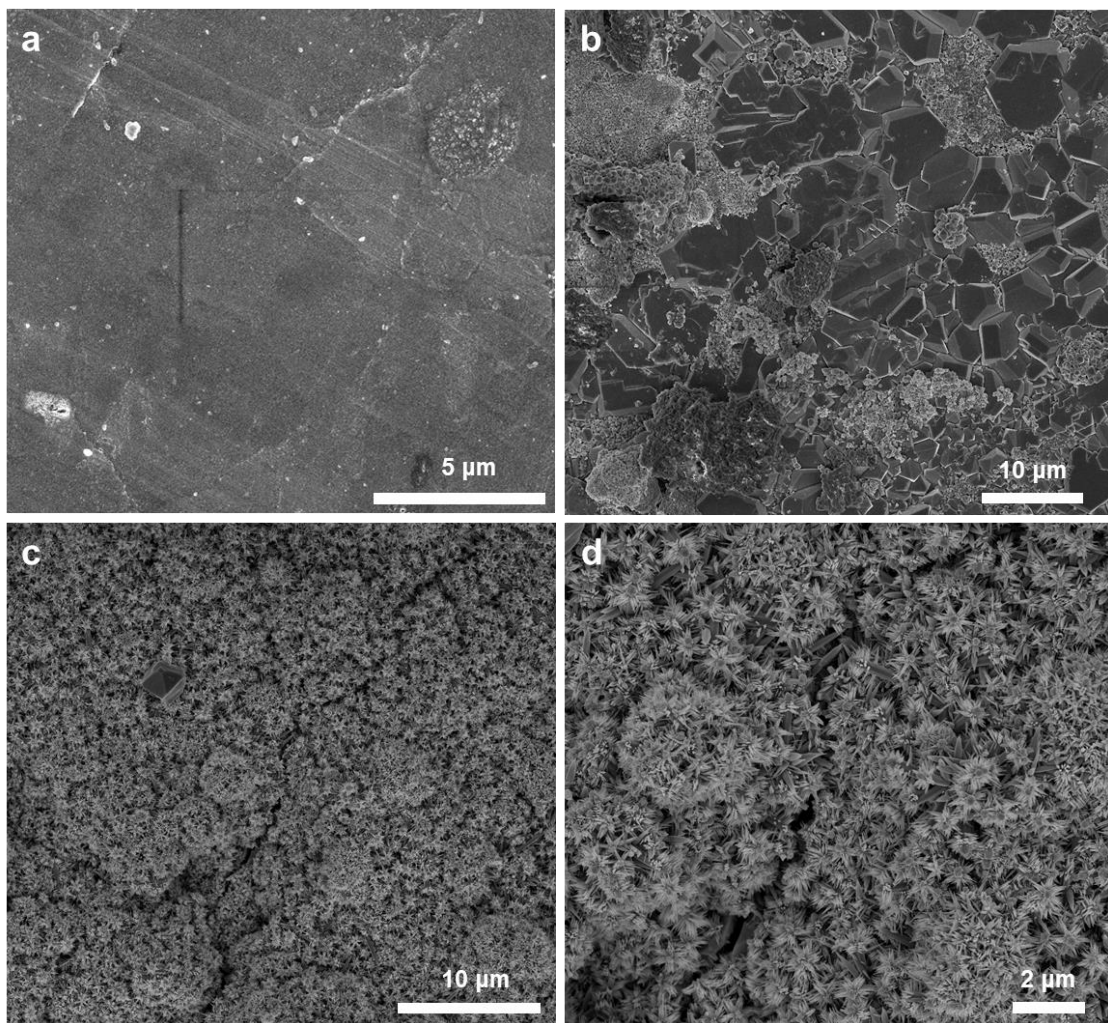


Fig. S44 SEM images of Fresh Zn foil (a), SEM images of Zn foil after cycling with C-CNF (b) and without C-CNF (c, d).

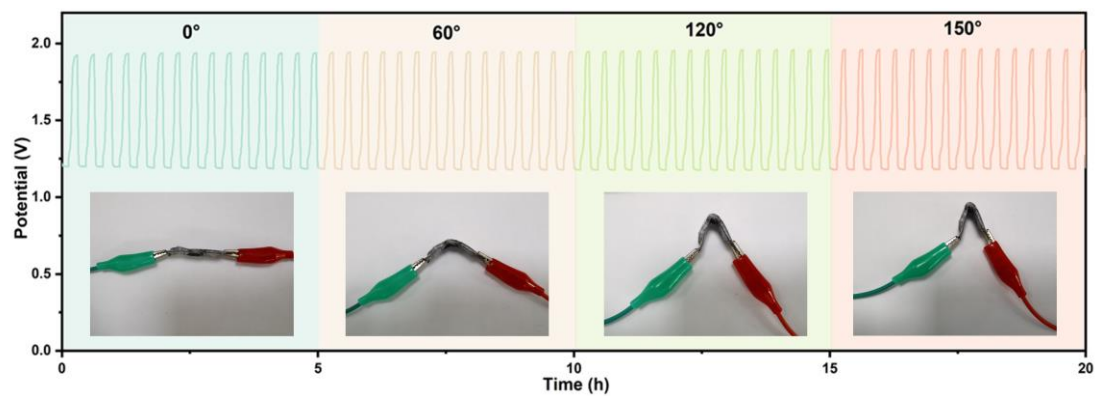


Fig. S45 Galvanostatic charge/discharge curves of Wood-WTF-ZABs in various bending states at a current density of 1 mA cm⁻².

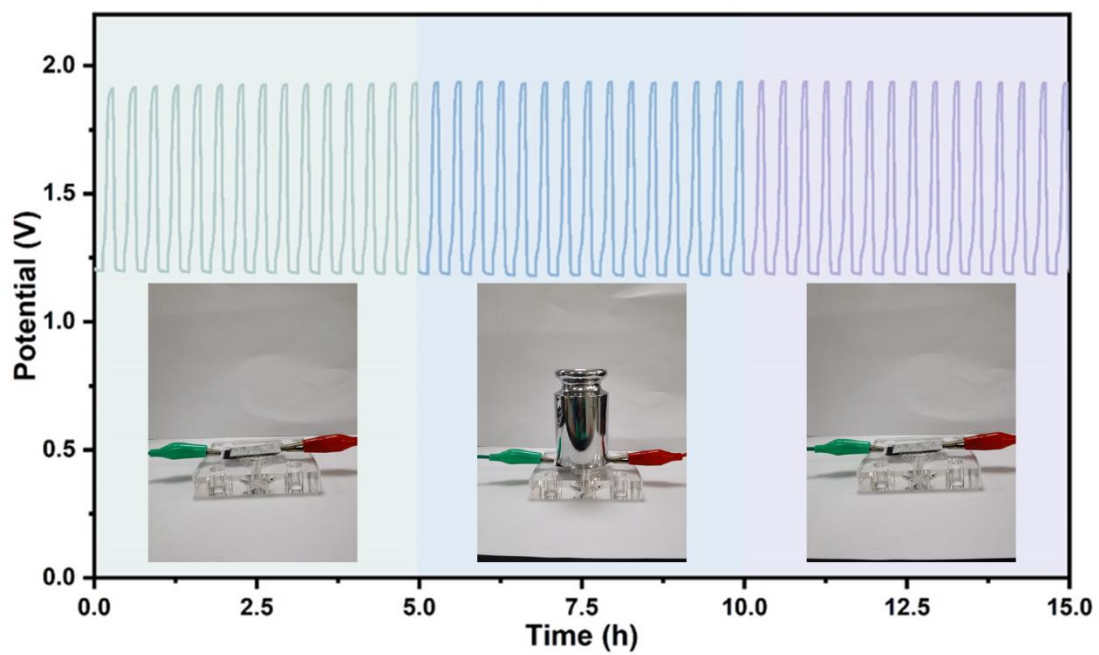


Fig. S46 Galvanostatic charge/discharge curves of Wood-WTF-ZABs with loading 500 g states at a current density of 1 mA cm⁻².

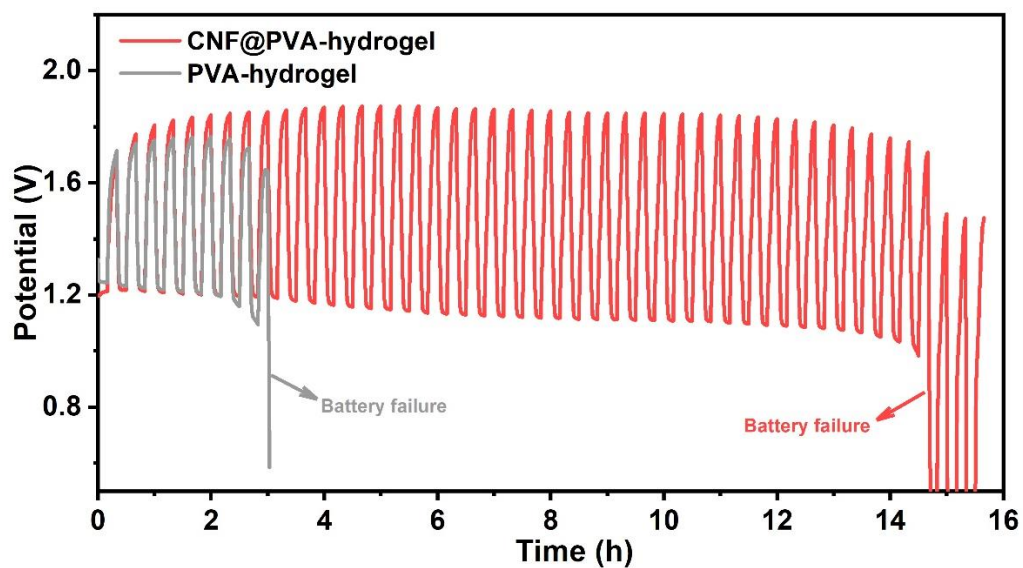


Fig. S47 Galvanostatic discharge/charge curves of PVA-hydrogel and CNF@PVA-hydrogel based batteries.

When DMSO was replaced by H₂O, the performance of flexible Zn-air batteries deteriorates considerably (only cycling for 14 h at 1 mA cm⁻², 20 min/cycle).



Fig. S48 (a) The potential of Wood-WTF-ZABs at low temperature; (b-c) an LEDs powered by two flexible Zn-air batteries at low temperature.

Notably, the absence of any reduction in luminance in the LEDs indicate that the ionic conductivity of the Wood-WTF-ZABs is affected minimally even in extremely low-temperature environments (Fig. S48, ESI†)

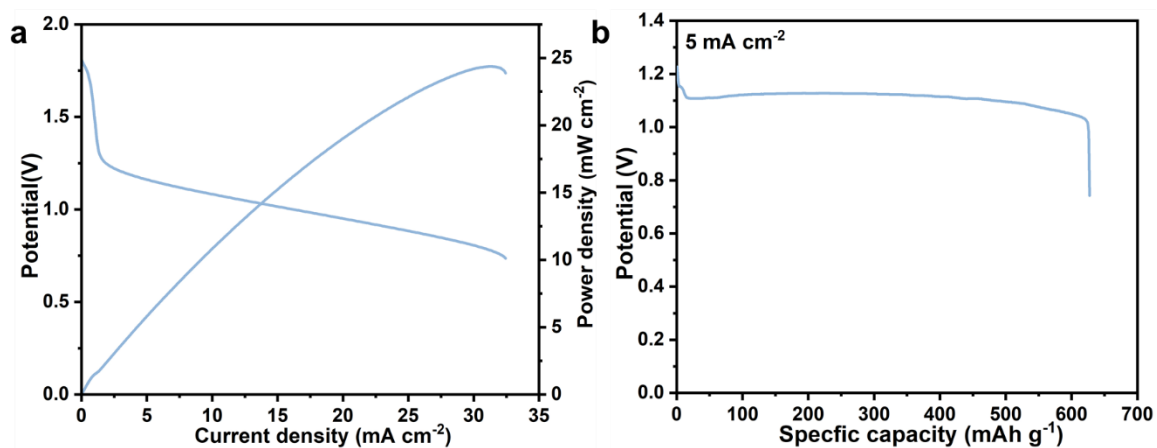


Fig. S49 Discharge polarization curves and power density (a) and galvanostatic discharge curves (b) of Wood-WTF-ZABs at -20°C .

Fig. S49 (ESI†) shows the peak power density and the specific capacity of Wood-WTF-ZABs at -20°C , which still possible to keep 25.2 mW cm^{-2} and 627.5 mAh g^{-1} , respectively.

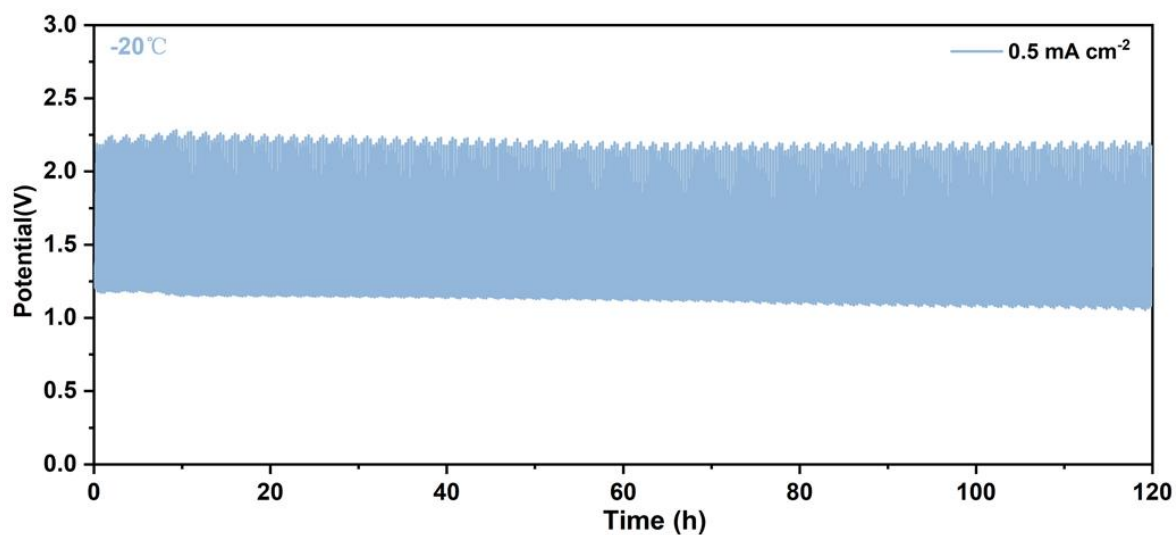


Fig. S50 Galvanostatic discharge/charge cycling curves of Wood-WTF-ZABs at 0.5 mA cm⁻² with a 20 min/cycle and operating in -20°C.

As shown in Fig. S50, the Wood-WTF-ZABs could cycling for more than 120 h at -20°C with 0.5 mA cm⁻².

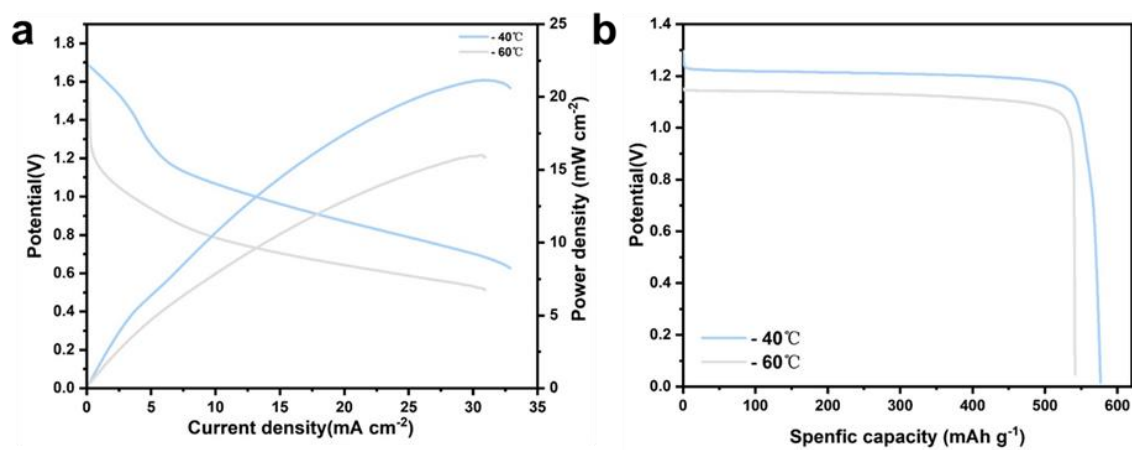


Fig. S51 (a) Discharge polarization curves and power density and (b) galvanostatic discharge curves of all wood based flexible Zn-air battery of Wood-WTF-ZABs at -40 and -60 °C.

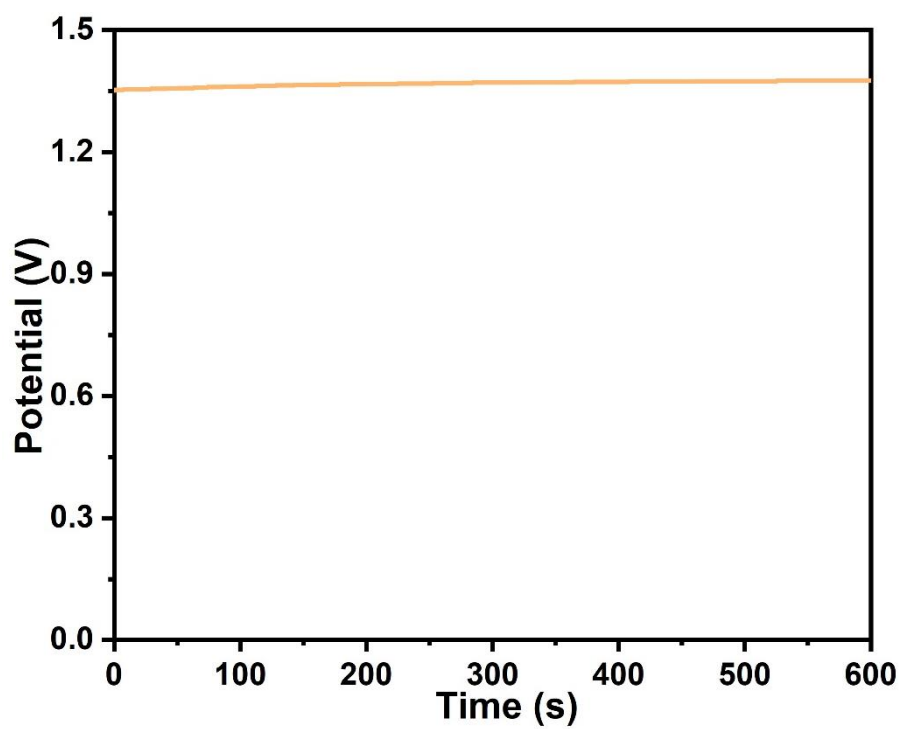


Fig. S52 The open-circuit potential of Wood-WTF-ZABs at 50°C.

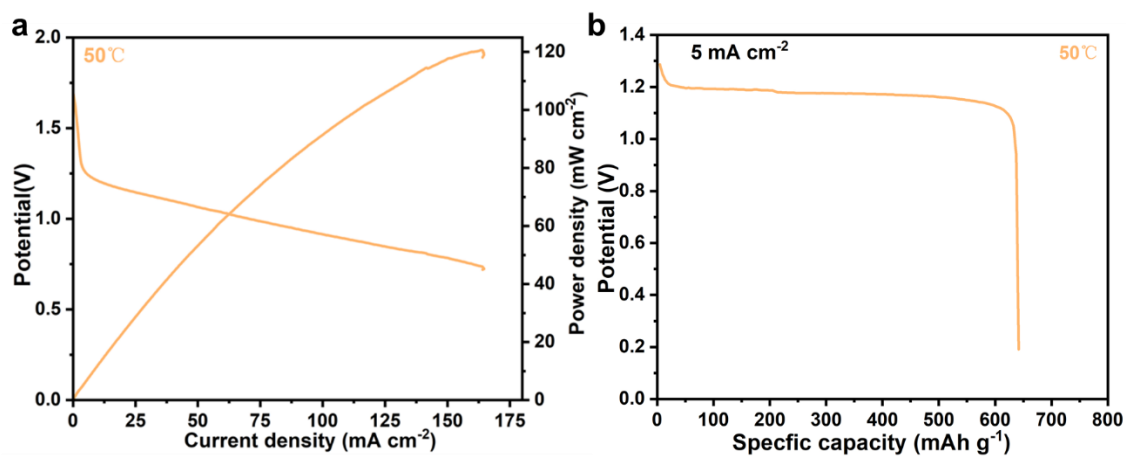


Fig. S53 (a) Discharge polarization curves and power density and (b) galvanostatic discharge curves of all wood based flexible Zn-air battery of Wood-WTF-ZABs at 50 °C.

As demonstrated in Fig. S49 (ESI†), the peak power density and the specific capacity of Wood-WTF-ZABs at 50°C attain 119 mW cm⁻² and 642 mAh g⁻¹, respectively.

Supplementary Table 1. Comparison of specific surface area of advanced Fe-based ORR catalysts has been reported.

| Catalyst | Specific surface area (m ² g ⁻¹) | Reference |
|---|---|---|
| Fe _x /FeN ₃ S ₁ -C | 1639.14 | This work |
| FeNC-EEB-2 | 731 | <i>Adv. Mater.</i> , 2023 , 35, 2208999 |
| Fe-N ₂ O/G | 273 | <i>Energy Environ. Sci.</i> , 2023 , 16, 2629–2636 |
| Fe SAs-MCP | 578.9 | <i>Nat. Com.</i> 2024 , 15:2062 |
| meso-FeNSC | 955 | <i>Nat Sustain</i> , 2024 . https://doi.org/10.1038/s41893-024-01300-2 |
| T-Fe SAC | 905 | <i>Angew. Chem. Int. Ed.</i> 2024 , e202319370 |
| Fe-N ₄ SP/NPS-HC | 1023.60 | <i>Energy Environ. Sci.</i> , 2024, 17(1): 249-259 |
| Fe SAs/NSC-vd | 708 | <i>Adv. Mater.</i> 2024 , 36, 2308243 |
| FeN ₄ -O-NCR | 1159 | <i>Adv. Mater.</i> 2022 , 34, 2202544 |
| Fe SA/NPCs | 388 | <i>Appl. Catal. B Environ.</i> 2020 . 278. 119270 |
| Fe _{AC} @Fe _{SA} N-C | 558 | <i>ACS Nano</i> 2019 , 13, 10, 11853-11862 |
| Fe/NC-3 | 773.9 | <i>Small Methods.</i> 2021 , 5, 2001165 |
| Fe-SAs/NSC | 547.6 | <i>J. Am. Chem. Soc.</i> 2019 , 141, 20118-20126 |
| SA-Fe ^{III} /SNPC | 1210 | <i>Adv. Funct. Mater.</i> 2023 , 2304277 |
| Fe SAs-Fe ₂ P | 1008.6 | <i>Adv. Mater.</i> 2022 , 34, 2203621 |

| | | |
|---|---------|---|
| Fe/Meso-NC-1000 | 848.4 | <i>Adv. Mater.</i> 2022 , 34, 2107291 |
| Fe _H -N-C | 1071 | <i>Adv. Mater.</i> 2023 , 35, 2210714 |
| FeN ₄ Cl ₁ /NC | 499 | <i>Angew. Chem. Int. Ed.</i> 2021 , 60, 27324 -27329 |
| Fe ₃ C@C-Fe SAS | 566 | <i>Nano Energy.</i> 2021 . 84. 105840 |
| Fe _{SA} -Fe _{NC} @NSC | 718.2 | <i>Small.</i> 2022 . 18. 2107225 |
| SAC-FeN-WPC | 1183.23 | <i>ACS Energy Lett.</i> 2021 .6. 3624-3633 |
| Fe ₃ C@NCNTs | 505 | <i>Energy Storage Materials.</i> 2022 . 51 149-158 |
| Fe SAs/NC | 1133.9 | <i>Adv. Mater.</i> 2023 , 35, 2209644 |

Supplementary Table 2. The atomic contents of C, N, O, S, Fe in $\text{Fe}_x/\text{FeN}_3\text{S}_1\text{-C}$ performed by XPS.

| Sample | Atomic levels (%) | | | | |
|--|-------------------|------|------|------|------|
| | C | N | O | S | Fe |
| $\text{Fe}_x/\text{FeN}_3\text{S}_1\text{-C-800}$ | 88.8 | 4.38 | 5.14 | 1.3 | 0.38 |
| $\text{Fe}_x/\text{FeN}_3\text{S}_1\text{-C-900}$ | 88.37 | 3.42 | 7.2 | 0.67 | 0.34 |
| $\text{Fe}_x/\text{FeN}_3\text{S}_1\text{-C-1000}$ | 90.9 | 1.55 | 6.84 | 0.27 | 0.43 |

Supplementary Table 3. The configuration of N dopant is determined from XPS N1s spectra.

| Sample | N Dopant (%) | | | | | |
|--|--------------|------|------------|-------------|------------|--------|
| | Pyridinic-N | Fe-N | Pyrrolic-N | Graphitic-N | Oxidized-N | Total% |
| Fe _x /FeN ₃ S ₁ -C-800 | 0.97 | 0.66 | 1.51 | 0.64 | 0.53 | 4.38 |
| Fe _x /FeN ₃ S ₁ -C-900 | 0.82 | 0.95 | 0.49 | 0.50 | 0.66 | 3.42 |
| Fe _x /FeN ₃ S ₁ -C-1000 | 0.39 | 0.89 | 0.26 | 1.12 | 0.28 | 2.93 |

Supplementary Table 4. EXAFS fitting parameters at the Fe K-edge for Fe_x/FeN₃S₁-C and FeN₃S₁-C

| Samples | path | C. N. ^[a] | R (Å) ^[b] | $\sigma^2 (\times 10^{-3} \text{ \AA}^2)$ ^[c] | R factor ^[e] |
|---|--------|----------------------|----------------------|--|-------------------------|
| Fe foil | Fe-Fe1 | 8* | 2.46±0.08 | 3.4±3.1 | 0.02 |
| | Fe-Fe2 | 6* | 2.85±0.08 | 6.2±4.1 | |
| Fe ₂ O ₃ | Fe-O | 5.8±0.9 | 1.97±0.02 | 9.1±2.6 | 0.02 |
| | Fe-Fe1 | 6.1±1.8 | 2.97±0.01 | 7.7±4.7 | |
| | Fe-Fe2 | 3.7±0.7 | 3.63±0.02 | 6.9±5.1 | |
| FePc | Fe-N | 3.8±1.6 | 1.96±0.01 | 6.4±4.8 | 0.02 |
| | Fe-Fe | 3.0±0.9 | 3.11±0.04 | 3.3±2.8 | |
| Fe _x /FeN ₃ S ₁ -C | Fe-N | 3.1±2.0 | 1.94±0.02 | 4.4±4.2 | 0.02 |
| | Fe-S | 1.2±1.1 | 2.27±0.02 | 6.1±5.0 | |
| | Fe-Fe | 2.1±1.1 | 2.89±0.02 | 7.3±3.8 | |
| | Fe-Fe | 6.1±1.5 | 3.27±0.02 | 15.1±5.8 | |
| FeN ₃ S ₁ -C | Fe-N | 3.8±0.9 | 1.94±0.02 | 9.5±2.8 | 0.02 |
| | Fe-S | 0.3±0.1 | 2.28±0.02 | 6.8±2.4 | |
| | Fe-Fe | 1.4±0.6 | 2.77±0.02 | 10.0±9.5 | |
| | Fe-Fe | 2.2±0.7 | 2.27±0.02 | 9.7±4.2 | |

^aCN, coordination number; ^bR, distance between absorber and backscatter atoms; ^c σ^2 , Debye-Waller factor to account for both thermal and structural disorders; ^d ΔE_0 , inner potential correction; ^eR factor indicates the goodness of the fit. A reasonable range of EXAFS fitting parameters: $CN > 0$; $\sigma^2 > 0 \text{ \AA}^2$; $R \text{ factor} \leq 0.02$.

Supplementary Table 5. The contrast of ORR performance between Fe_x/FeN₃S₁-C catalyst and other reported advanced catalysts in 0.1 M KOH.

| Catalyst | Mass loading ($\mu\text{g cm}^{-2}$) | E _{onset} (V vs. RHE) | E _{1/2} (V) (V vs. RHE) | Reference |
|---|---|-----------------------------------|-------------------------------------|---|
| Fe _x /FeN ₃ S ₁ -C | 255 | 1.01 | 0.90 | This work |
| Fe/N-CNRs | 400 | 1.10 | 0.90 | <i>Adv. Funct. Mater.</i> 2021 , 31, 2008085 |
| FePC & rGO | 459 | 0.98 | 0.89 | <i>Energy Storage Materials.</i> 2022 .50 12-20 |
| Fe-N-C | 459 | — | 0.895 | <i>Applied Catalysis B: Environmental.</i> 2022 . 313 121454 |
| Fe-NSDC | 255 | 0.96 | 0.84 | <i>Small.</i> 2019 , 15, 1900307 |
| Fe-N/P-C-700 | 300 | 0.941 | 0.867 | <i>J. Am. Chem. Soc.</i> 2020 , 142, 2404-2412 |
| FeN/CS-1000 | 250 | 0.98 | 0.86 | <i>ACS Sustainable Chem. Eng.</i> 2022 , 10, 7031-7040 |
| Fe ₂ N@NCNT | 612 | — | 0.86 | <i>ACS Sustainable Chem. Eng.</i> 2022 , 10, 9105-9112 |
| Fe ₃ C@N/MCHSs | 306 | 1.01 | 0.875 | <i>Adv. Funct. Mater.</i> 2022 , 32, 2200397 |
| 3DOM Fe-N-C-900 | 612 | — | 0.875 | <i>Nano Energy</i> 2020.71. 104547 |

| | | | | |
|---------------|-----|------|------|---|
| FeNSFs | 280 | — | 0.84 | <i>Carbon.</i> 2022. 187. 196e206 |
| Fe SA-NSC-900 | 100 | 0.94 | 0.86 | <i>ACS Energy</i> <i>Lett.</i> 2021 , 6, 379-386 |
| Fe-Fe@NC | 255 | 0.95 | 0.82 | <i>Nanoscale</i> <i>Horiz.</i> 2020. 5. 359-365 |
| Fe/NC-3 | 255 | 0.97 | 0.90 | <i>Small Methods</i> 2021. 5. 2001165 |

Supplementary Table 6 Calculated Gibbs free energies of ORR elementary step forFe₄/FeN₃S₁-C, FeN₃S₁-C, Fe₄-FeN₄-C and FeN₄-C.

| Elementary reactions | | I | II | III |
|---|----------|--|---|-------------------------------------|
| | | OOH*+H ₂ O+OH ⁻ +3e ⁻ | O*+H ₂ O+2OH ⁻ +2e ⁻ | OH*+3H ⁺ +e ⁻ |
| Fe ₄ /FeN ₃ S ₁ -C | U=0 V | -1.08 | -2.95 | -4.08 |
| | U=1.23 V | 0.15 | -0.49 | -0.39 |
| FeN ₃ S ₁ -C | U=0 V | -1.31 | -3.34 | -4.33 |
| | U=1.23 V | -0.14 | -0.91 | -0.63 |
| Fe ₄ -FeN ₄ -C | U=0 V | -1.26 | -3.17 | -4.25 |
| | U=1.23 V | -0.03 | -0.71 | -0.56 |
| FeN ₄ -C | U=0 V | -1.44 | -3.57 | -4.39 |
| | U=1.23 V | -0.21 | -1.11 | -0.70 |

Supplementary Table 7. Comparison of Zn–air battery performance for some reported non-noble metal catalysts.

| Catalyst | Electrolyte | Open Circuit Voltage (V) | Peak Power Density (mW cm ⁻²) | Capacity (mAh g ⁻¹) | Discharge/Charge Stability | Reference |
|---|------------------------------------|--------------------------|---|---------------------------------|---|---|
| Fe _x /FeN ₃ S ₁ -C | 6 M KOH/0.2 M Zn (AC) ₂ | 1.46 | 249 | 767 | 20 mA cm ⁻² , 425 h 5 mA cm ⁻² , 600 h | This work |
| Fe/N-CNRs | 6 M KOH | 1.44 | 181.8 | 771.77 | 10 mA cm ⁻² , discharge 100 h | <i>Adv. Funct. Mater.</i> 2021 , 31, 2008085 |
| FePC & rGO | 6 M KOH/0.2 M Zn (AC) ₂ | 1.34 | 103 | 739.7 | 5 mA cm ⁻² , 600 s/cycle, 800 cycles | <i>Energy Storage Materials.</i> 2022 .50 12-20 |
| Fe-N-C | 6 M KOH/0.2 M Zn (AC) ₂ | 1.479 | 175 | 775.7 | 5 mA cm ⁻² , 10 min/cycle, 3860 cycles | <i>Applied Catalysis B: Environmental.</i> 2022 . 313 121454 |
| Fe-NSDC | 6 M KOH/0.2 M Zn (AC) ₂ | 1.53 | 225.1 | 740.8 | 4 mA cm ⁻² , 10 min/cycle, 3860 cycles | <i>Small.</i> 2019 , 15, 1900307 |
| Fe-N/P-C-700 | 6 M KOH/0.2 M Zn (AC) ₂ | 1.42 | 133.2 | 723.6 | 10 mA cm ⁻² , 40 h | <i>J. Am. Chem. Soc.</i> 2020 , 142, 2404-2412 |
| FeN/CS-1000 | 6 M KOH/0.2 M Zn (AC) ₂ | — | 115 | 742 | 5 mA cm ⁻² , 22 min/cycle, 600 cycles | <i>ACS Sustainable Chem. Eng.</i> 2022 , 10, 7031-7040 |
| Fe ₂ N@NCNT | 6 M KOH/0.2 M Zn (AC) ₂ | 1.53 | 135 | 762 | 5 mA cm ⁻² , 200 h | <i>ACS Sustainable Chem. Eng.</i> 2022 , 10, 9105-9112 |
| Fe ₃ C@N/MC HSs | 6 M KOH/0.2 M Zn (AC) ₂ | 1.5 | 95 | 810 | 60 h | <i>Adv. Funct. Mater.</i> 2022 , 32, 2200397 |

| | | | | | | |
|-----------------|--|------|-----|-------|--|---|
| 3DOM Fe-N-C-900 | 6 M KOH | 1.45 | 235 | 768.3 | 5 mA cm ⁻² , discharge 100 h | <i>Nano Energy</i> 2020.71. 104547 |
| FeNSFs | 6 M KOH/0.2 M Zn (AC) ₂ | 1.84 | 173 | 717 | 20 mA cm ⁻² ,165 h | <i>Carbon.</i> 2022 .187. 196e206 |
| Fe-Fe@NC | 6 M KOH | 1.45 | 175 | 675 | 5 mA cm ⁻² , discharge 30 h | <i>Nanoscale</i> <i>Horiz.</i> 2020 . 5. 359-365 |

Supplementary Table 8. Diffusivities of OH⁻ and H₂O of CNF@PVA-SSE

| | OH ⁻ diffusivity | H ₂ O diffusivity |
|-----------------------|--------------------------------------|--------------------------------------|
| | × 10 ⁵ cm ² /S | × 10 ⁵ cm ² /S |
| diffusion coefficient | 0.0074 | 0.1305 |

Supplementary Table 9. Comparison of flexible Zn–air batteries performance for some reported.

| Catalyst | Gel electrolyte | OCP (V) | Peak Power Density (mW cm ⁻²) | Cycle duration (h)@current density (mA cm ⁻²) | Reference |
|--|------------------------|---------|---|---|--|
| Fe _x /FeN ₃ S ₁ -C | CNF@PVA-SSE | 1.46 | 157 | 200@1; 115@5 90@10 50@20 | This work |
| NCNF film | PVA | 1.26 | - | 6@2 | <i>Adv. Mater.</i> 2023 , 35, 2209644 |
| Mn ₃ O ₄ /NiCo ₂ S ₄ | PVA-PEO | 1.43 | - | 16.8@1 | <i>J. Power Sources</i> 2020 , 462, 228162. |
| Air electrode (PF04) | P18@PAA | 1.45 | 154.48 | 36@2 | <i>Adv. Funct. Mater.</i> 2023 , 2303719 |
| Pt/C + RuO ₂ | MXene/Zn-LDH-array@PVA | 1.37 | 92.3 | 50@3 | <i>Adv. Energy Mater.</i> 2022 , 12, 2201393 |
| Mn-Co-Fe@CNT | M-Agar gel | 1.46 | 126 | 25@2 | <i>Chemical Engineering Journal.</i> 2023 . 452 139301 |
| FeN/CS-1000 | KI-PVAA-GO | 1.43 | 78.6 | 200@2 | <i>Adv. Mater.</i> 2020 , 32, 1908127 |
| Co-N-CCNFMs/CC | KOH/PANa | 1.46 | 61.5 | 37@2 | <i>Energy Storage Materials.</i> 2022 . 47 (2022) 365-375 |
| FeP/Fe ₂ O ₃ @NP CA | PVA | 1.42 | 40.8 | 8.3@5 | <i>Adv. Mater.</i> 2020 , 32, 2002292 |
| (Zn,Co)/NSC | PVA | 1.56 | 15 | 0.42@0.1 | <i>Adv. Mater.</i> 2020 , 32, 2002292 |
| CoNi-CoN ₄ -HPC-900 | PVA | 1.5 | 116 | 27@5 | <i>Nano Energy.</i> 2022 . 99. 107325 |

| | | | | | |
|---------------------------------------|----------------|------|-------|--------|---|
| S-C ₂ NA | Cellulose | 1.47 | 187 | 460@25 | <i>ACS Nano.</i> 2018 , 12, 596-608 |
| Fe/Fe ₃ C@NdC-NCs | P-(AM-co-AA) | 1.43 | 60 | 40@5 | <i>J. Mater. Chem. A.</i> 2019 , 7, 17581-17593 |
| Commercial cobalt oxide nanoparticles | CCNF-PDIL SSE | 1.46 | 135 | 240@2 | <i>Angew. Chem. Int. Ed.</i> 2022 , 61, e202117703(10 of 11) |
| NPCNF-O | PVA | 1.46 | 105.7 | 130@1 | <i>ACS Catal.</i> 2022 , 12, 4002-4015 |
| CNT paper | PANa-Cellulose | 1.48 | 80 | 110@5 | <i>Adv. Energy. Mater.</i> 2019 , 9, 1803046 |

Supplementary Table 10. Comparison of wide-temperature flexible Zn–air batteries

performance for some reported.

| Catalyst | Gel electrolyte | Operating temperature (°C) | Battery performance-Cycling time (h)@ current density (mA cm ⁻²) @ temperature (°C) | Reference |
|--|--------------------------------------|----------------------------|---|--|
| Fe _x /FeN ₃ S ₁ -C | CNF@PV A-SSE | -60-50 | 114@0.5@-40 40@0.5@-60 34@0.5@50 | This work |
| CoSe ₂ - NCNT NSA | PAA | 0-40 | 5@2@ 0, 25 and 40 | <i>Nanoscale</i> , 2021 , 13, 3019-3026 |
| PEMAC @NDCN | Chitosan biocellulos ics | -40-70 | 91.5@25@-40 96.4@25@70 | <i>Nano-Micro Lett.</i> 2022 .14:190 |
| Fe ₃ Co ₇ - NC | PAA | -30-60 | 2000 cycles@2@-30 330 cycles@2@60 | <i>Adv. Funct.</i> <i>Mater.</i> 2023 , 33, 2212299 |
| Ni/N- ESC | PAA | -20-25 | 100 cycles@3@-20 500 cycles@3@25 | <i>Energy Storage</i> <i>Materials.</i> 2022 . 47.235-248 |
| SV-900 | C20E2G5 | -40-60 | 200@2@20 | <i>Small.</i> 2023, 2302727 |
| FeCo- NPC | PAA | -20-25 | 100@5@-20 | <i>Energy Storage</i> <i>Materials.</i> 2023 . 59. 102772 |
| Co ₉ S ₈ - NSAB | PANa- PVA-IL | -40-60 | 200@2@-20 105@2@60 | <i>Adv. Mater.</i> 2023 , 35, 2209980 |
| Pt/C and RuO ₂ | Temperatu re-tolerant hydrogel | -20-25 | 30 cycles@1@70 100 cycles@1@25 | <i>ACS Sustainable</i> <i>Chem. Eng.</i> 2020 , 8, 11501-11511 |
| FeCo- Mo _{0.82} N | PAM-CNF gel | -10-40 | | <i>ACS Appl. Mater.</i> <i>Interfaces.</i> 2023 . 15. 15344-15352 |
| FeNi- NPC | PAA | -20-25 | 40 cycles from 25 to 20 and recover to 25 | <i>Journal of Energy</i> <i>Chemistry.</i> |

| | | | | |
|----------------|-------------------------------|--------|--|---|
| Pt/C+Ir/ C | CsOH- based electrolyte | -10-20 | 160 cycles@5@; 65 cycles@10@-10 °C; | <i>Angew. Chem. Int. Ed.</i> 2021 , 133, 15409 -15413 |
| BFC-FC- 0.2 | A-PAA | -20-25 | 105@2@25 from 25 to 20 and recover to 25 | <i>Angew. Chem. Int. Ed.</i> 2020 , 59, 4793-4799 |
| CMN- 231H | PAMC | -20-25 | 190 cycles@5@-20 | <i>Chemical Engineering Journal.</i> 2021 , 417 .129179 |
